Thermal-infrared radiosity and heat-diffusion model for estimating sub-pixel radiant temperatures over the course of a day

Iryna Danilina

A dissertation
submitted in partial fulfillment of
the requirements for the degree of

Doctor of Philosophy

University of Washington

2012

Reading Committee:
Alan Gillespie, Chair
Joshua Bandfield
Stephen Warren

Program Authorized to Offer Degree:
Department of Earth and Space Sciences

University of Washington

Abstract

Thermal-infrared radiosity and heat-diffusion model for estimating sub-pixel radiant temperatures over the course of a day

Iryna Danilina

Chair of the Supervisory Committee:

Professor Alan Gillespie
Department of Earth and Space Sciences

In temperature/emissivity estimation from remotely measured radiances the general assumption is that scene elements represented by pixels in fact have a single emissivity spectrum and are isothermal. Thus, estimated temperatures and emissivities are the effective values that would be found if these simplified assumptions were met. In reality, the physical scene is neither homogeneous nor isothermal, and the effective values are not strictly representative of it. This dissertation is devoted to thermal-infrared radiosity and a heat-diffusion model used for predicting effective emissivity spectra and radiant temperatures for rough natural surfaces, which allows one to estimate discrepancies between effective and actual values. Computer model results are compared to analytic model results in order to verify that the computer model is working properly. The model is validated against spectra measured in the field using a hyperspectral imaging spectrometer and a cm-scale DTM of the test scene acquired using a tripod-based LiDAR. The discrepancies between analytical and modeled values are less than 0.01%. Modeled emissivity spectra deviate from the measured by no more than 0.015 emissivity units. Modeled kinetic temperature on average deviates from measured by less than 1K over the course of a day. Possible applications of the developed model in remote sensing, planetary science, and geology are described.

TABLE OF CONTENTS

LIST OF FIGURES ii

LIST OF TABLES iv

Chapter 1:Introduction 1

Chapter 2: Thermal-infrared radiosity and heat-diffusion model 10

2.1 Approach and data 10

2.2 Radiosity model 12

2.3 Model verification 19

Chapter 3: Validation of TIR radiosity and heat-diffusion model performance 22

Chapter 4: TIR radiosity and heat-diffusion model results 29

Chapter 5: Applications of TIR radiosity and heat-diffusion model 37

5.1 Compensation for sub-pixel roughness effects in TIR images 37

5.2 3-D modeling of icy landscape evolution on Callisto 45

5.3 Solar stresses and fractures in exposed rocks 47

Chapter 6: Summary 50

Bibliography 544

LIST OF FIGURES

1 Hyperspectral TIR images and derived emissivity spectra.....5

2 Examples of field data used 11

3 Schematic plot illustrating terms used in the form-factor equations .....

.....15

4 Schematic plot illustrating geometry assumed in the apparent emissivity calculation for the case of radiation between a single surface element and a large finite wall, parallel to the element. 20

5 Gabbro rock validation experiment results. 24

6 Plaster template validation experiment results. 25

7 Heat-diffusion part of the model validation experiment results. 27

8 Averaged modeled emissivity over the course of a day for alluvial surfaces of different roughness 30

9 Effect of surface RMS on $\Delta\varepsilon$ in alluvial, bedrock, and lava flow surfaces. 31

10 The radiosity model results for a granite bedrock surface. Part 1. 32

11 The radiosity model results for a granite bedrock surface. Part 2. 33

12 Generalized transfer functions for alluvial, bedrock and lava flow surfaces ..35

13 Flow chart illustrating approach to compensation for sub-pixel roughness effects in TIR images. 39

14 Comparison of RMS roughness images derived from RADAR image and using two-look method. 41

15 Example of the results of the approach to compensation for sub-pixel roughness effects in TIR images. 43

16 High resolution Galileo images showing landscape evolution on Callisto. 46

17 Examples of modeled and measured kinetic temperatures used in solar stresses and fractures in exposed rocks study. 48

LIST OF TABLES

1 Comparison of analytical and model calculations of the apparent emissivity 21

ACKNOWLEDGEMENTS

I have really enjoyed my years in University of Washington. The Department of Earth and Space Sciences is a great place to start a scientific career. Faculty and grad students in the Department are extremely intelligent and versatile and always ready to jump into discussion of any scientific or non-scientific topic. I want to thank members of my PhD Supervising Committee, and particularly my advisor Alan Gillespie. Besides the top-notch research advice, he always gave me a lot of support on the personal level. I also would like to express eternal gratitude to my family in Ukraine for love and support they gave me in everything I have ever done. My husband Dmytro has been a constant source of support, inspiration, and love for me. I would like to sincerely thank him for that.

This research was supported by subcontract PR32449 from Los Alamos National Laboratory and contract DE-FG52-08NA28772/M001 from the NNSA program, U. S. Department of Energy.

CHAPTER 1: INTRODUCTION

In recent decades remote sensing has become an important instrument for geological and environmental research, especially by providing access to previously inaccessible or dangerous areas not only on Earth, but on other planets as well. In particular, thermal-infrared (TIR) remote sensing is commonly used for soil development, erosion studies, etc. Remotely sensed TIR data is used to determine land surface kinetic temperatures and emissivities. In turn, the latter are a common diagnostic of surface composition, especially in the case of the silicate minerals that make up much of the land surface (Gillespie *et al.,* 1998). Therefore, accurate determination of surface emissivities is of primary importance.

In TIR imaging it is necessary to integrate the radiant flux from the scene over the pixel projected on the ground, and then use one of several algorithms (*e.g.*, Gillespie *et al*., 1998; Wan & Li, 1997; Sobrino & Li, 2002; Jiménez-Muñoz *et al*., 2006) to estimate effective temperatures and emissivities for the surface. For multispectral data and under the assumptions that the surface is smooth, homogeneous, and isothermal, values of the effective parameters are commonly within a degree or two, or within ~0.015 emissivity units, of the values measured *in situ* (*e.g.,* Gillespie *et al.,* 1998). A primary goal of this doctoral research is to quantify what happens if these fundamental assumptions are violated. These answers

will become even more important as technology improvements allow imaging with increasingly higher spatial and radiometric resolutions.

Some studies have addressed simplified versions of the general surface heterogeneity problem. Dozier (1981) estimated snow cover assuming that the pixel represented a binary mixture of snow-covered and bare components; Pieri *et al.* (1990) applied similar reasoning to determine temperatures for unresolved lava effusions viewed against a background of cooled lava; and Gustafson *et al*. (2003) considered extraction of temperatures of unresolved stream elements. All these studies used the simplifying assumption that the scene consisted of two unresolved components, each homogeneous. Gillespie (1992) considered the more general case in which the scene contained multiple spectral endmembers, but nevertheless assumed each pixel was isothermal. Ramsey & Christensen (1992, 1998) also modeled spectral mixtures, but used linear mixtures of emissivities rather than spectral radiances. Several terrestrial studies investigated the effects of assuming an isothermal field of view (FOV) on TIR data (e.g. Balick and Hutchinson, 1986; Smith *et al.,* 1997; Zhang *et al.,* 2004; McCabe *et al.,* 2008). These studies have typically focused on the effects of vegetation and directionality on surface temperatures derived from broadband measurements. Due to the fact that variation on sub-pixel scale is primarily due to vegetation rather than slopes on bare surfaces, the anisothermality were not linked to roughness. Bandfield, 2009 investigated slopes in martian apparent surface emissivity observations collected by the Thermal Emission Spectrometer (TES) and Thermal

Emission Imaging System (THEMIS). This slopes were attributed to misrepresenting the surface temperature, either through incorrect assumptions about the maximum emissivity of the surface materials or the presumption of a uniform surface temperature within the FOV.

In this research, I investigate the dispersion of temperatures and emissivities that occur as the assumed conditions – that scene elements are isothermal and smooth – are relaxed. Previous studies have used simulated scenes to address this problem. However, Weeks *et al.* (1996) showed that although roughness parameterizations (e.g., root-mean-squared (RMS) roughness, elevation mean values) of random noise and natural scenes might be the same, the temperature/emissivity (T/ε values calculated by retrieval algorithms outputs might differ. Therefore, simulated terrain must be used with caution. Here I report on the findings relevant to radiant temperature, from analysis of thermal-infrared images (TIR: 8 – 14 μm) and digital terrain models (DTMs) at the 1 – 10 cm scale, the scale at which the basic building blocks, such as gravel and jointed bedrock, of the landscape are resolved. The discussion is restricted to unvegetated surfaces.

Thermal-infrared ground-leaving radiance comprises direct ground-emitted radiance and reflected radiance from the atmosphere and neighboring scene elements. The reflected radiance reduces the apparent emissivity contrast ("cavity effect") in remotely estimated emissivity spectra because reflectivity ρ and emissivity ε are complementary (Kirchhoff's law). By 'emissivity contrast' I mean the range of

emissivity values within a spectrum. For an ideal cavity, approximated in figure 1(*a*) by a mine adit (coarse scale) and in figure 1(*c*,*d*) by cracks in a rock (fine scale), the TIR radiance spectrum figure 1(*b*) approaches that of an ideal blackbody, regardless of composition.

If roughness at either topographic or subpixel scales is not accounted for in image analysis, it is possible to confuse rough surfaces with smooth surfaces of intrinsic low emissivity contrast, or with mixtures of rocks having high and low emissivity contrast. Uncorrected, these ambiguities can lead to uncertainty in surface compositions and abundances inferred from remotely acquired thermal images. Not taking roughness effects into account may also lead to inaccurate estimation of surface kinetic temperatures, which are important for energy-balance studies.

Cavity effects from resolved, coarse-scale topography can be corrected with a DTM and a TIR radiosity model, but effects from unresolved cavities require a more elaborate protocol because the fine-scale roughness cannot be measured directly from remote-sensing data. Compensation for this latter effect of subpixel roughness on thermal images does not appear to have previously accomplished. Another goal of this research is therefore to define an approach for accounting for fine-scale cavity effects in thermal images of natural surfaces, and to test it with high-resolution field data.

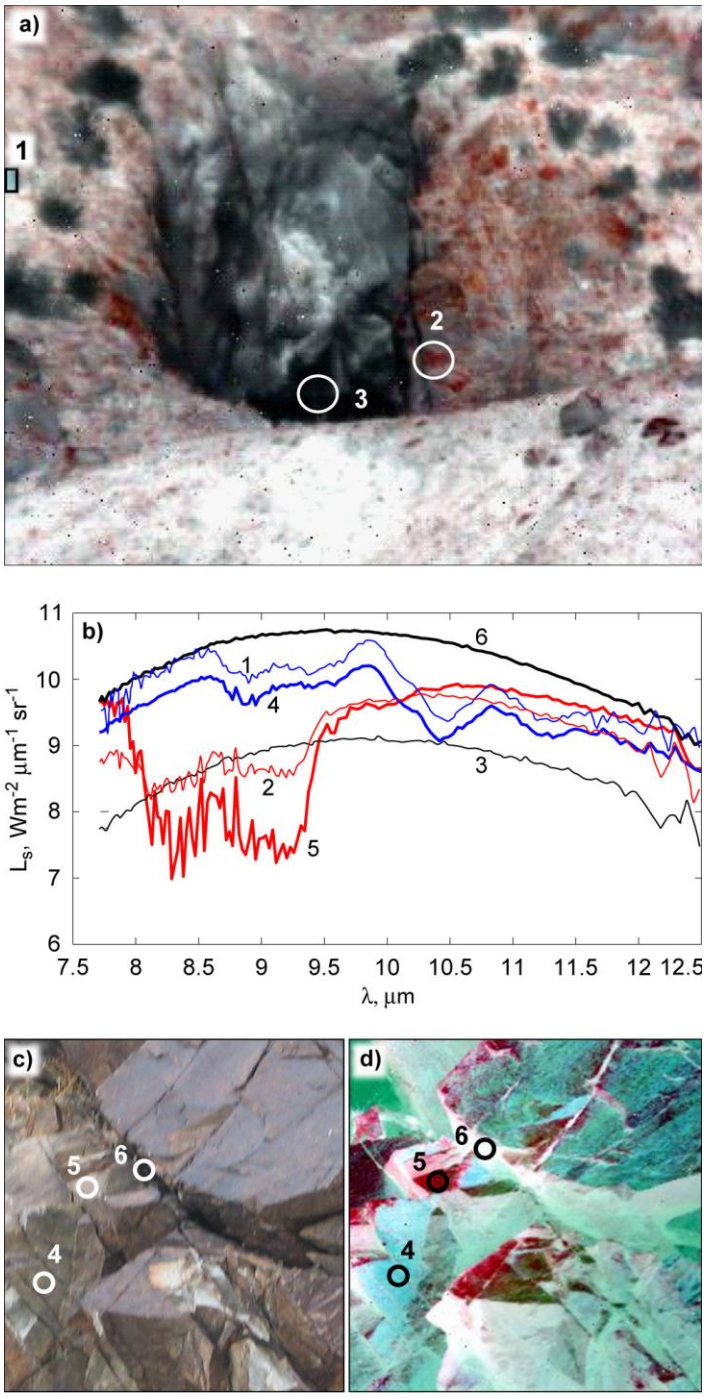

Figure 1. Telops, Inc., Hyper-Cam TIR data, Owens Valley, CA, USA (range: ~25 m). a) False-color image ~10 m across (RGB= 10.87, 8.59, 8.26 μm). b) Radiance spectra of schistose (1) and quartzite (2) wall rocks, the adit (3), schistose (4) and quartzite (5) parts of a 1 m rock fallen from the cliff, and deep cracks in the rock (6). c) Photo of the rock (range: ~9 m; image is ~80 cm across). d) False-color TIR image of the same rock (RGB same as in a).

This dissertation consists of following parts. In Chapter 2, a radiosity model adapted for TIR measurements and coupled with a heat-diffusion model is presented. Radiosity is the total radiance from the surface element, consisting of energy emitted by this surface element directly and the energy reflected from adjacent surface elements. Radiosity models for visible and near- and shortwave-infrared wavelengths include reflected direct sunlight (Li, 1997), but this term is negligible in the TIR. The model presented in this dissertation takes into account the effects of a surface geometry, changing illumination geometry, thermo-physical and spectral properties of the surface material, multiple-scattering effects, sensible heat transfer at the surface-air boundary, and downwelling sky radiation. I assume all differential surface elements are Lambertian: perfect diffusers that emit and reflect radiation isotropically. Chapter 2 contains description of the model and verification of its performance for simple analytical case.

Chapter 3 focuses on the model validation. Well-controlled detailed thermal observations on natural and artificial surfaces were used for validation. The strategy was then to reproduce calculated and observed effects with the radiosity model. Three validation experiments were conducted using a simply shaped gabbro rock as well as a physical model made of Plaster of Paris ($CaSO_4 \bullet 2H_2O \pm CaCO_3$).

In Chapter 4 model results are presented. Distributions of kinetic temperatures and radiosities over the course of day and night were calculated for a set of natural surfaces of different types, such as alluvial surfaces, bedrock, and lava flows. An

example of the results for a bedrock surface is demonstrated. Transfer functions relating the contribution of cavity radiation from landscape elements of different roughnesses were defined for different types of natural surfaces.

Chapter 5 discusses applications for the developed TIR radiosity and heat-diffusion model. The main application is compensation for sub-pixel roughness effects in TIR images. The model has also been used for 3-D modeling of icy landscapes evolution on the Gallilean and Saturnian satellites and kinetic temperature predictions for solar stress and fracture in exposed rocks. Finally, Chapter 6 gives brief summary of the research described in this dissertation.

I use the term 'emissivity' throughout the dissertation. Here I give an explanation of different types of emissivity and symbols used for each of them. Emissivity is defined as the ratio between the measured surface-emitted radiation and the radiation expected from a blackbody at the same kinetic temperature. The emissivity of a material (ε) is an emissivity value that would be measured for a smooth surface. 'Apparent emissivity' (ε_{app}) is an emissivity value for a rough surface estimated from measured spectral radiance without correction for cavity effect. 'Modeled apparent emissivity' (ε_{mod}) is an emissivity value for a rough surface represented by a DTM and includes the effects of multiple reflection and cavity radiation. I calculate ε_{mod} from the spectral radiance estimated by the TIR radiosity model presented here. The qualitative difference between ε_{mod} and ε_{app} is that ε_{mod} is not affected by roughness at scales finer than resolved by the DTM, whereas ε_{app} is

influenced by roughness at all scales. Ideally, correction for the cavity effect should allow one to calculate ε from ε_{app}**,** provided that all other corrections were done accurately. The difference between modeled and 'material' emissivity is designated as $\Delta\varepsilon = \varepsilon_{mod} - \varepsilon$.

Finally, the content of this dissertation is based on the following papers:

- Danilina, I., Mushkin, A., Gillespie, A. R., O'Neal, M. A., Abbott, E. A., Pietro, L. S., Balick, L. K., 2006. Roughness effects on sub-pixel radiative temperature dispersion in a kinetically isothermal surface. *Abstract Book, Conference on Recent Advances in Quantitative Remote Sensing II (RAQRS II)*, University of Valencia, Spain, Sept. 25-29, p. 31.

- Danilina, I., Gillespie, A., Smith, M., Balick, L., Abbott E., 2010. Thermal infrared radiosity and heat diffusion model verification and validation. *Proceedings of the 2nd Workshop on Hyperspectral Image and Signal processing: Evolution in Remote Sensing*, Reykjavik, Iceland, 14-16 June.

- Danilina, I, Gillespie, A, Balick, L., Mushkin, A., Smith, M., Blumberg, D, 2012. Compensation for subpixel roughness effects in thermal infrared images, *International Journal of Remote Sensing*, in press.

- Danilina, I, Gillespie, A, Balick, L., Mushkin, A., O'Neal, M., 2012. Performance of TIR radiosity and heat-diffusion model for subpixel

radiant temperature estimation over the course of a day, *Remote Sensing of Environment*, in press.

CHAPTER 2: THERMAL-INFRARED RADIOSITY AND HEAT-DIFFUSION MODEL

In this chapter a radiosity model adapted for TIR and coupled with a heat-diffusion model is presented. First, a short description of types of data used for model calculations and validation is given. The main part of the chapter is dedicated to the detailed description of the developed model. Finally, the model performance is verified with a simple analytical case.

2.1 Approach and data

Natural scenes used in my experiments were 0.5-m to 10-m bedrock and alluvial landscapes in the Mojave Desert, California, USA (Death Valley and Owens Valley). At each field site, I generated high-resolution digital terrain models (DTMs) (0.5 – 5 cm resolution) from tripod-mounted LiDAR (Trimble GS200) measurements. I developed the radiosity model for predicting over the course of a day the temperature effects due to scene roughness, and used radiosity rather than a ray-tracing approach because, although computationally expensive, it is better suited for Lambertian surfaces and its results are independent of the observer position (Goral *et al.,* 1984). Hyperspectral TIR images of selected sites were measured at

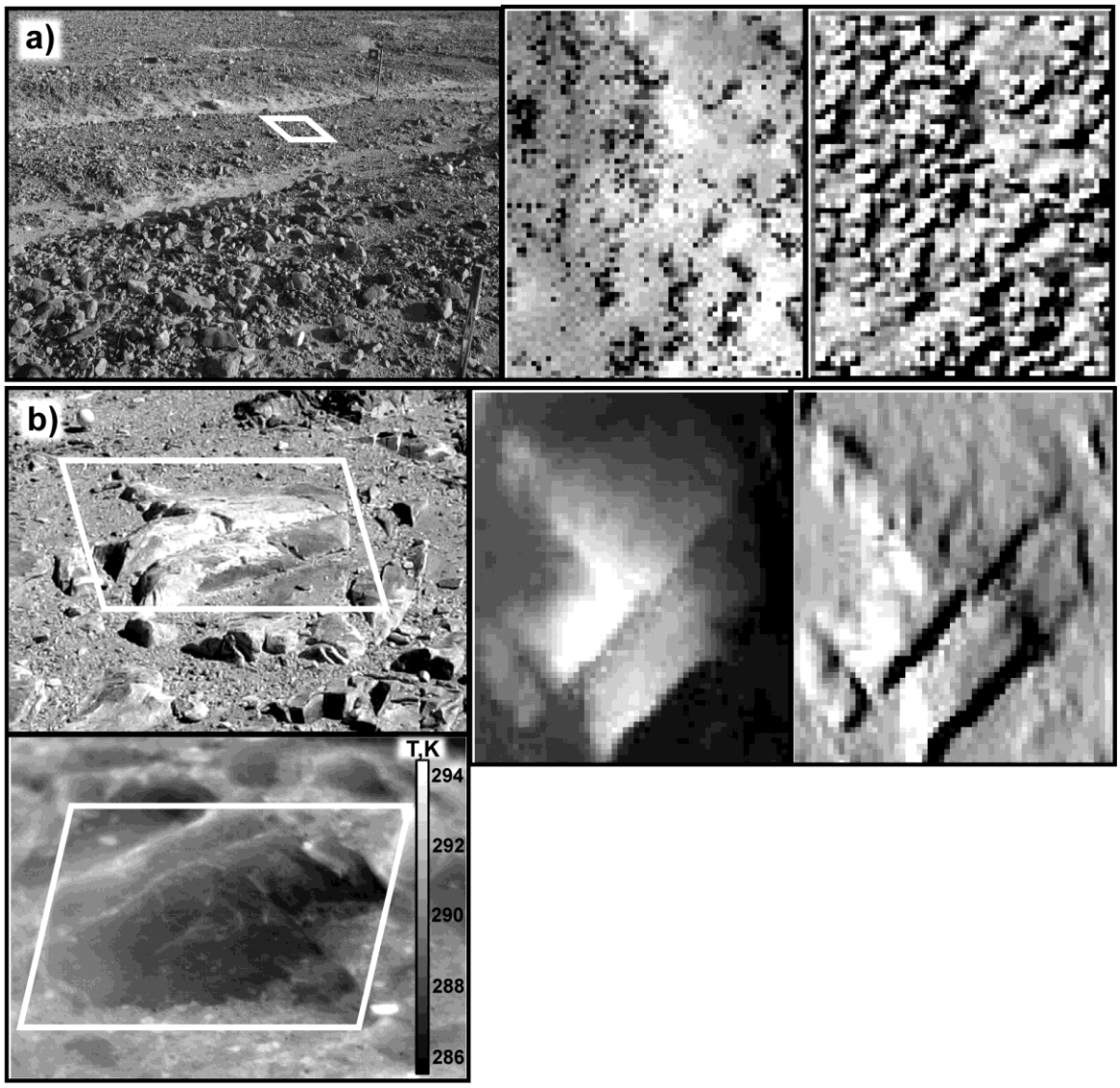

Figure 2. Examples of data used. a) Alluvial fan surface (Death Valley). From left to right: photo of the surface, DTM of the surface (surface size is 0.6 m by 0.75 m, DTM resolution is 1 cm, number of pixels is 4636), shaded relief image. b) Natural bedrock surface (Owens Valley). From left to right: photo of the surface, DTM of the surface (surface size is 1.16 m by 1.36 m, DTM resolution is 2 cm, number of pixels is 3944), shaded relief image. On the bottom there is the oblique broad-band image of the surface made by FLIR camera taken at 17:00. Note different perspective of the FLIR image compared to the photo and DTM.

various view angles and times of day using the Telops Inc. First Hyper-Cam sensor. I also acquired radiant-temperature images using a FLIR broadband TIR camera (FLIR Systems Inc.) with NEΔT$\approx$0.3 K. Images made before sunup and during the day were used for testing the model predictions. FLIR data were used whenever hyperspectral Hyper-Cam data were unavailable. Examples of data used are given in Figure 2.

2.2 Radiosity Model

In this research, I consider the case of thermal radiance from a homogeneous surface during the course of a day, including effects of changing illumination geometry, thermo-physical properties of the surface material, multiple-scattering effects, sensible heat transfer at the surface-air boundary, and downwelling sky radiation. I assume all surface elements are Lambertian: perfect diffusers that emit and reflect radiation isotropically, according to Lambert's law ($L = \rho\ I\ cos\varphi$, where L is the reflected radiance, ρ is the surface reflectivity, I is the irradiance, and φ is the angle between the illuminating ray and the local surface normal, or the incidence angle). This study makes use of the wavelength range from 8 μm to 14 μm (i.e., the 'thermal' part of the spectrum). Emissivity is generally regarded as independent of temperature. Here for simplicity I describe the basic form of the radiosity model formulated with the assumption that our surfaces are graybodies within this interval: *i.e.*, ε is independent of wavelength. Modifications of the model, capable of accommodating surfaces with different spectral signatures in the TIR spectral region,

were also developed and used for various calculations, including model validation experiments described below.

The general form of a radiosity model in our case is written as:

$$B_i = R_i + MS_i, \qquad i = 1,2\ldots n, \tag{1}$$

where B_i, W/m^2 – radiosity of a surface element i;

R_i, W/m^2 – thermal energy emitted from a surface element;

MS_i, W/m^2 – multiple-scattering component (energy bounced one or more times among surface elements);

n – number of surface elements.

The radiation emitted by a blackbody surface at any given wavelength is described by Planck's Law. But natural surfaces usually do not behave as perfect emitters, so Planck's function must be modified by including ε. Thus, the hemispheric spectral radiance emitted from each surface element is given by

$$R_i = \varepsilon \cdot \int_{\lambda_1}^{\lambda_2} \frac{c_1}{\lambda^5} \cdot \frac{1}{e^{c_2/\lambda T_i} - 1} \cdot d\lambda, \quad i = 1,2\ldots n, \tag{2}$$

where $c_1 = 3.74 \cdot 10^{-16}\, W \cdot m^2$ – first radiation constant;

$c_2 = 0.0144\ m \cdot K$ – second radiation constant;

$\lambda_1 = 8 \cdot 10^{-6}\ m$ – lower limit of the thermal part of the spectrum;

$\lambda_2 = 14 \cdot 10^{-6}\ m$ – upper limit of the thermal part of the spectrum;

T, *K* – kinetic temperature of a surface element.

The main complication of the radiosity model is the calculation of the multiple-scattering component. The amount of energy reflected from adjacent surface elements is determined by their geometric relation, which can be established using slope and aspect information derived from high-resolution DTMs. This geometric relation is called the "form factor" and is defined as fraction of energy leaving one surface element and reaching another (Sparrow, 1963; Sparrow & Cess, 1978).

The full radiosity model is written as:

$$B_i = R_i + \rho \cdot \sum_{j=1}^{n} B_j \cdot F_{ij}, \quad i, j = 1,2 \ldots n, \tag{3}$$

where ρ – reflectivity of a surface;

F_{ij} – dimensionless form factor from surface element *j* to surface element *i*.

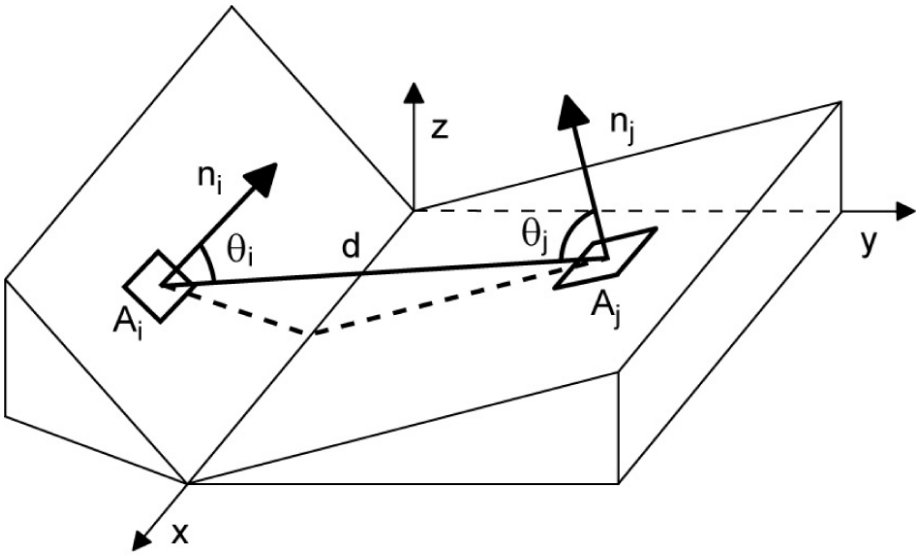

Figure 3. Schematic plot illustrating terms used in the form-factor equation.

There are *n* unknown radiosities and *n* linear equations associated with individual pixels. Rearranging equation (3), the *n* linear equations can be written in a matrix expression:

$$\begin{bmatrix} 1-\rho F_{11} & \dots & -\rho F_{1n} \\ -\rho F_{21} & \dots & -\rho F_{2n} \\ \vdots & & \vdots \\ -\rho F_{n1} & \dots & 1-\rho F_{nn} \end{bmatrix} \cdot \begin{bmatrix} B_1 \\ B_2 \\ \vdots \\ B_n \end{bmatrix} = \begin{bmatrix} R_1 \\ R_2 \\ \vdots \\ R_n \end{bmatrix} \tag{4}$$

For the surfaces elements with a modeled temperature, *R* is calculated using Planck's Law (equation 2). The key step of the radiosity model is determining the form-factor matrix *F*. The basic equation for a form-factor is

$$F_{ij} = \frac{\cos\theta_i \cdot \cos\theta_j}{d^2 \cdot \pi} \cdot dA_i, \quad (5)$$

where F_{ji} – form factor from surface element; *j* to surface element *i*;

θ – projection angle between the normal of a surface element and line, linking the pair of elements together;

A_i, m^2 – area of element *i*;

d, m – the distance between two elements.

Using equation (5), the form-factor matrix F (eqn. 3 – 5) can be constructed. Terms from equation (5) are illustrated in Figure 3.

In order to incorporate heating by the sun into the model several steps are necessary. First, for daytime, solar radiation on the surface is modeled. It depends on the changing position of the sun (elevation and azimuth) over the course of a day, geometry of the surface, and atmospheric conditions (air temperature, cloud fraction, and other factors). The geometry of the surface determines the solar radiation incidence angles for each given sun position, as well as which surface elements are illuminated. Using the DTMs, a matrix containing this information is formed. For night time this first step is not required.

Second, the kinetic temperature for each surface element has to be determined. In order to do this, the thermal inertia of the material needs to be considered. This amounts to considering heat flow inside the material. For simplicity I neglect the three-dimensional nature of the heat diffusion and consider only the flux normal to the surface of the material. This process is described with the 1-D (vertical) heat-diffusion equation.

$$\frac{\partial T(z,t)}{\partial t} = k \frac{\partial^2 T(z,t)}{\partial z^2}, \tag{6}$$

where z, m – depth in the temperature profile,

t, s – heating time,

k, m^2/s – thermal diffusivity of the material.

Then, the surface heat-balance equation, including incoming solar radiation, downwelling sky radiation, sensible heat, energy losses for the radiation from the surface, heat flux into a material, and multiple-scattering component, is used as a boundary condition on the surface.

$$\alpha(T_{air} - T) + \varepsilon S_{\downarrow} + \varepsilon_{vis} I_0 \cos(i) + \frac{\varepsilon}{(1-\varepsilon)} MS - \varepsilon\sigma T^4(0,t) + \kappa \frac{\partial T(0,t)}{\partial z} = 0, \tag{7}$$

where α, $W/(m^2 \cdot K)$ – heat transfer coefficient,

T_{air}, K – ambient air temperature,

$S_{\downarrow}$, W/m^2 – downwelling sky radiation,

ε_{vis} – surface emissivity in the VNIR part of the spectrum.

I_0, W/m^2 – incoming solar radiation flux,

φ – incidence angle of solar radiation,

MS, W/m^2 – multiple scattering component,

σ, $W/(m^2 \cdot K^4)$ – Stefan-Boltzmann constant,

κ, $W/(m \cdot K)$ – thermal conductivity.

The heat-transfer coefficient and downwelling sky radiation term can be estimated empirically (Zhang *et al.,* 2004*;* Brutsaert, 1975). As main part of solar energy incident on the surface is concentrated in visible and near infrared (VNIR) part of the spectrum, it is necessary to use appropriate value of emissivity ε_{vis} in the part of the surface boundary condition describing incoming solar energy. Value of ε_{vis} is normally different from ε. The lower boundary condition is considered to be constant temperature at some appropriate depth below the level reached by the diurnal heating wave (i.e. ~20 cm for dry soils). Here, the model uses 25 1 cm layers in order to estimate surface kinetic temperature and temperature profiles below the surface.

Finally, a matrix representing the kinetic temperature of each surface element is used as an input parameter for the previously described radiosity model to get a new distribution of radiant temperatures over a given surface. The steps discussed above have to be repeated for different sun positions (each one using the results of the previous one as its initial condition) in order to investigate dispersion of radiant temperatures over the course of a day. For day time, change in the sun position and new temperature and radiosity distributions are calculated every 30 minutes. For night time, time step only depends on ambient air temperature change.

2.3 Model verification

For the model verification I used a simple case of radiation between a single surface element (referred to as element from now on) and a large finite wall, parallel to the element and facing it. The element and wall had the same temperature and emissivity. The distance between the element and the wall must be large compared to the element size. This was an analytic model, not a physical model. Simple geometrical considerations provide the apparent emissivity, $\varepsilon_{app,}$ of the element as a function of its emissivity, ε

$$\varepsilon_{app} = \varepsilon\left(1+\rho\int_{-X/2}^{X/2} dx \int_{-Y/2}^{Y/2} dy \frac{h^2}{\pi(h^2+x^2+y^2)^2}\right), \tag{8}$$

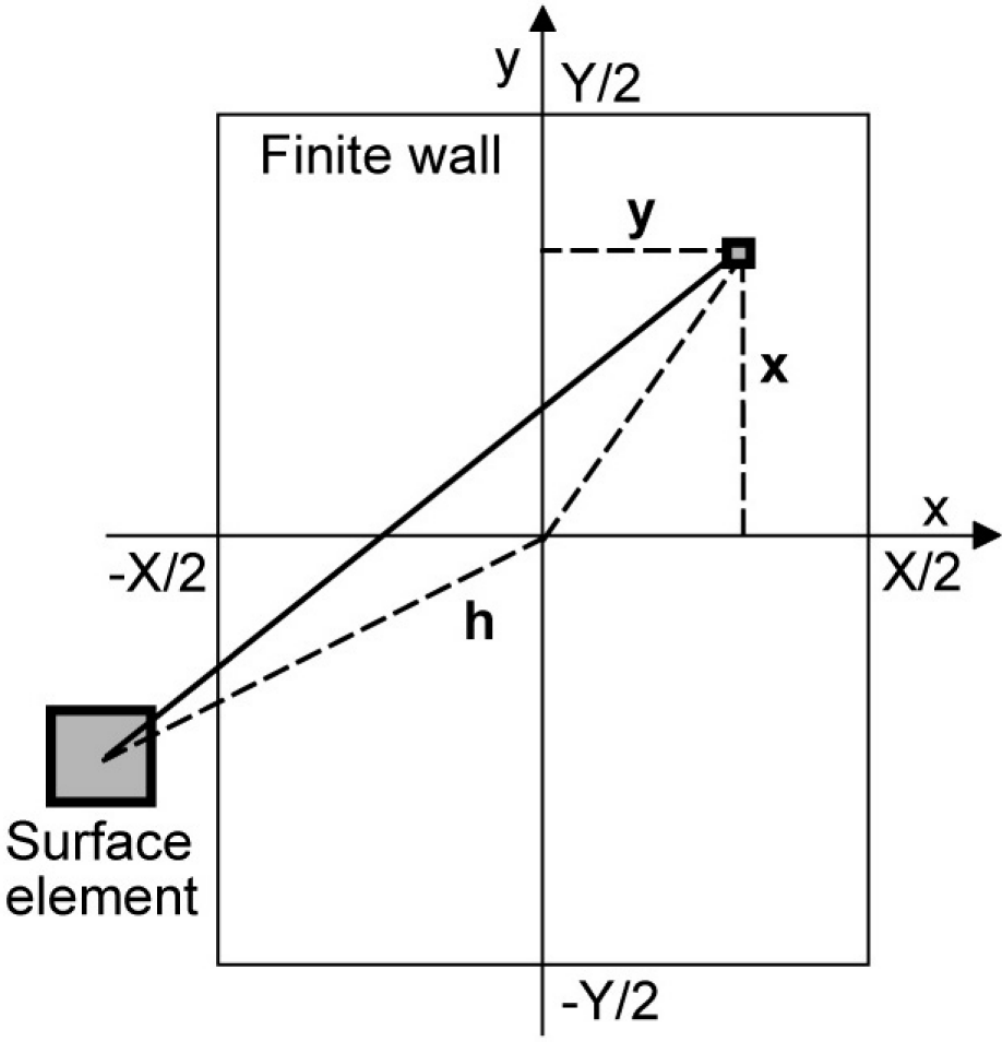

Figure 4. Schematic plot illustrating geometry assumed in the apparent emissivity calculation for the case of radiation between a single surface element and a large finite wall, parallel to the element.

Here $\rho=1-\varepsilon$ is the reflectivity of the wall and the element, and the meaning of geometrical parameters h, X and Y, entering Equation 8 is illustrated in Figure 4. Note that $\varepsilon_{app}=\varepsilon=1$ in the case of the black body ($\varepsilon=1, \rho=0$)

I also generated a DTM for the described layout, and compared the radiosity model results to the analytic solution. For all considered wall sizes the errors between modeled and analytical values were less than 0.01% (Table 1).

Table 1. Comparison of analytical and model calculations of the apparent emissivity ($\varepsilon = 0.87$); error is defined as $(\varepsilon_{\mathrm{mod}} - \varepsilon_{app}) / \varepsilon_{app}$. Distance between the wall and the element was 0.022 m, while the element size was 0.002 m by 0.002 m.

Wall size, cm	**Analytical calculation**	**Model calculation**	**Error, %**
2 by 5	0.9097	0.9096	0.0070
3 by 7.5	0.9293	0.9294	0.0095
4 by 10	0.9432	0.9432	0.0006

In his chapter, the developed radiosity model adapted for TIR and coupled with a heat-diffusion model was presented. I also described field data used in the study and demonstrated that the model performs as expected in the verification experiment. Next, it is necessary to validate the model with field measurements before any applications. This is the main focus of Chapter 3.

CHAPTER 3: VALIDATION OF THE TIR RADIOSITY AND HEAT-DIFFUSION MODEL PERFORMANCE

This chapter is dedicated to validation of TIR radiosity and heat-diffusion model performance. Whereas verification described in section 2.3 focuses on determining whether the developed code performs as expected, in other words answers the question "Is the model built right?", validation answers the question "Is the built model right?", i.e. demonstrates model's ability to accurately simulate real world processes. For the model validation well-controlled detailed thermal observations of natural and artificial surfaces were used. The strategy was then to reproduce calculated and observed effects with the radiosity model.

For the first of the validation tests of the model I used Hyper-Cam hyperspectral images of a rectangular hypersthene gabbro rock (dominantly ortho-pyroxene and calcic plagioclase) with a relatively smooth surface into which two holes had been drilled (Fig. 5). This simple cylindrical cavity allowed me to easily trace the effect that surface geometry has on the temperature, radiosity, and apparent emissivity during the course of a day, and also facilitated analytical estimation of this effect.

Hypersthene gabbro has overlapping Reststrahlen bands in the TIR, the main ones being at 8.67 and 9.9 μm according to ASTER spectral library

(http://speclib.jpl.nasa.gov/speclibdata/jpl.nicolet.rock.igneous.mafic.solid.ward41.spectrum.txt). Apparent emissivity spectra were recovered from the Hyper-Cam images using contact temperatures measured with thermocouple at the time of image acquisition. For the smooth surface of the rock there is a dip in the recovered spectrum that deepens from ~ 0.94 at the sides to ~ 0.89 in the middle of the spectrum. In the drilled holes however, the spectrum has significantly reduced contrast. Thus, the cavities drilled on the gabbro surface approximate blackbodies due to the multiple scattering inside them. My goal was to reproduce this effect within the radiosity model.

The rock measurements were about 18 cm by 10 cm by 6 cm. The holes were approximately 3 cm deep and 2 cm in diameter. A DTM of the rock with 2-mm resolution was measured with NextEngine 3-D scanner for use in the radiosity model. In the calculation ε was prescribed to have a value of 0.89 (depth of the Reststrahlen band measured with Hyper-Cam). Figure 5e shows modeled emissivity distribution over the rock surface. Spectral contrast is reduced inside the cavities and ε_{mod} increases up to 0.95. This shows good qualitative and quantitative agreement between the model results and the measurements.

For another validation experiment I created a simply shaped physical model from Plaster of Paris ($CaSO_4 \bullet 2H_2O \pm CaCO_3$). To avoid confusion with usage of the word ‘model’ I will call it ‘plaster template’ from now on. The surface of the plaster

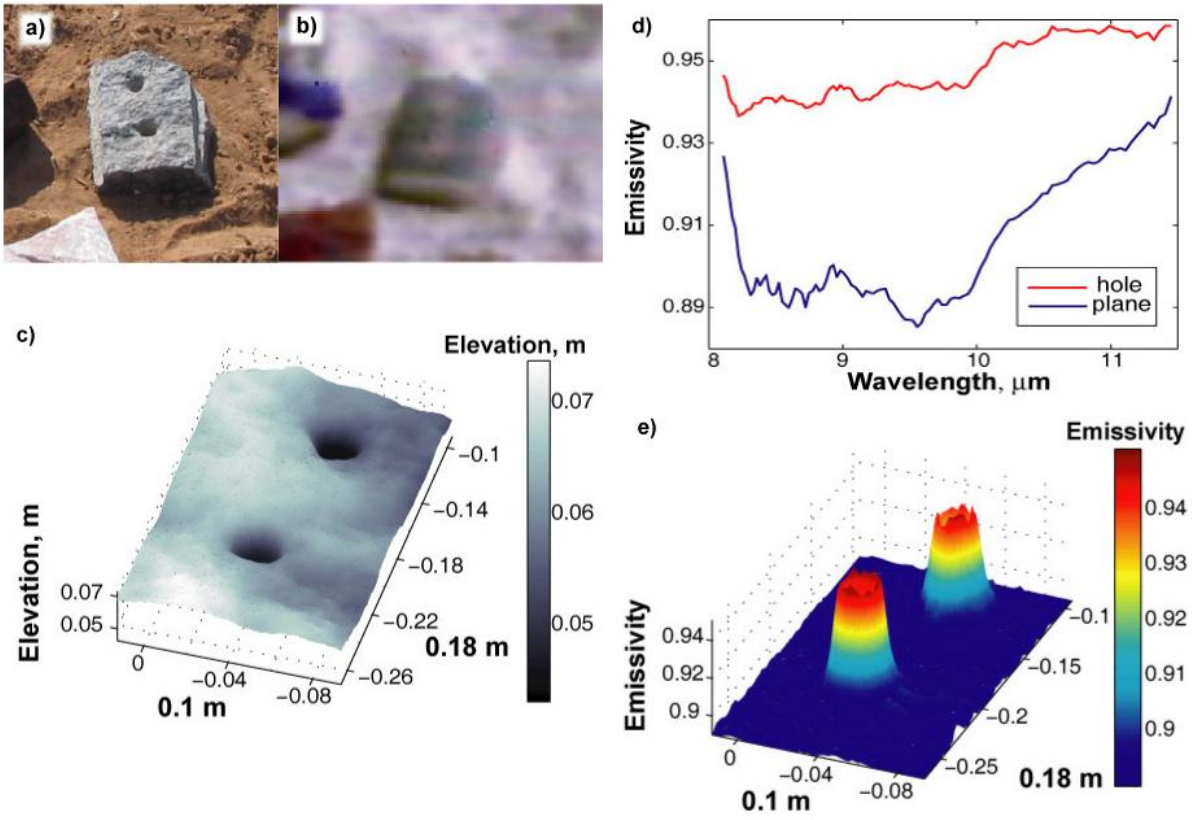

Figure 5. a) Photo of the gabbro rock in the field. b) Hyper-Cam image of the rock, RGB = 9.6, 8.9, 8.3 μm. c) Perspective view of the rock surface. d) Spectra estimated from Hyper-Cam measurements. e) ε_{mod} *calculated by the model. For this example,* ε *of the surface was 0.89.*

template had two horizontal planes connected by a vertical wall ~7 cm high. The upper plane had a cavity ~8 cm deep and ~3 cm in diameter (Fig. 6a). The plaster has a single Reststrahlen band centered near 8.6 μm. Measured in the field, ε_{app} in the band was as low as ~0.84; ε_{app} of the continuum spectrum was ~0.94.

For the experiment the plaster template was placed on an ~east-facing slope of about 30° (Figure 6). Hyper-Cam hyperspectral images of the surface were measured over the course of a day. From these, both ε_{app} and radiant temperatures of

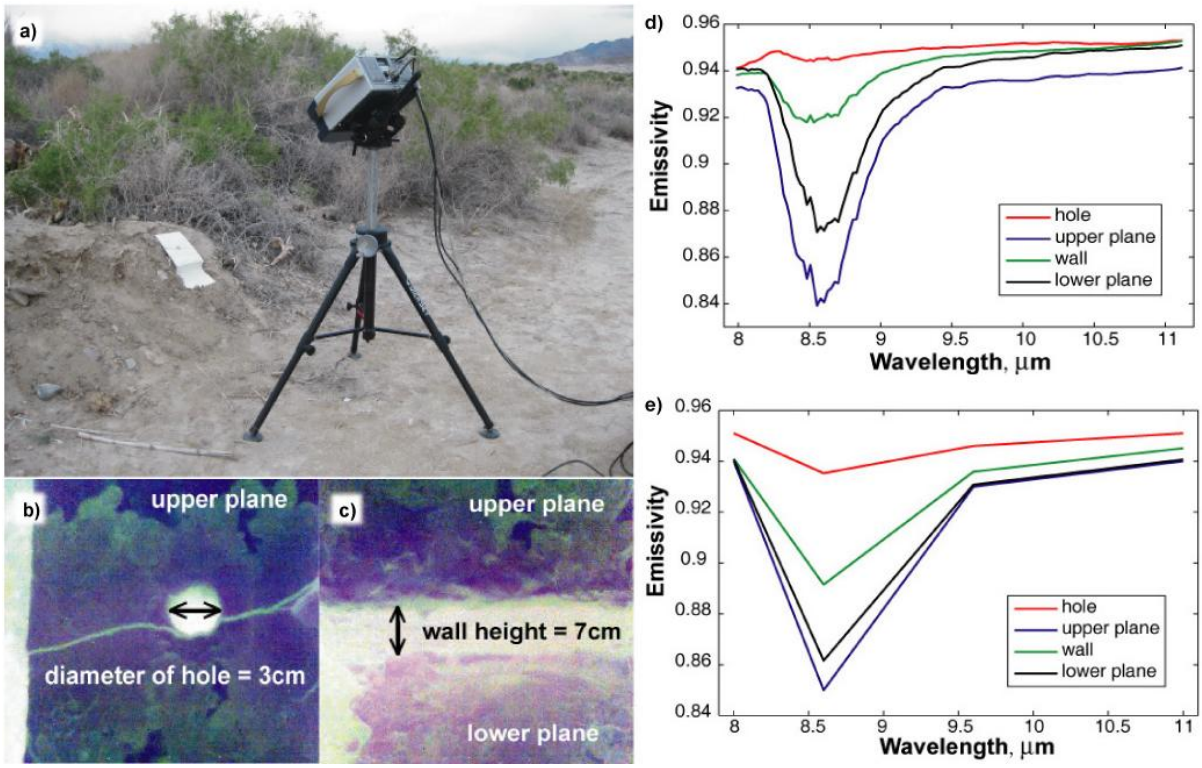

Figure 6. a) Hyper-Cam imaging spectrometer measuring the plaster template in the field. b) Hyper-Cam close up of the upper plane of the plaster template, with the hole. c) Hyper-Cam close up of the wall and the lower plane of the plaster template. For b) and c) RGB = 8.0, 8.7, 10.0 µm. Color differences on the planes are due to the texture of the surface. The diagonal line in b is a crack in the plaster. d) ε_{app} spectra from Hyper-Cam measurements. e) ε_{mod} spectra calculated by the model for four wavelengths: 8.0, 8.6, 9.6, and 11.0 µm.

surface elements were derived to demonstrate changes due to solar heating and multiple reflection among elements at different kinetic temperatures.

I generated a 3-mm/pixel synthetic DTM of the plaster template from its measured dimensions, slopes and aspects, and used it to drive the radiosity model. I prescribed the ε at four wavelengths (8.0, 8.6, 9.6, and 11.0 µm) as the value measured for the flat plaster surface (ε = 0.94, 0.85, 0.93, and 0.94, respectively). These wavelengths

were chosen because they capture the basic spectral shape and comprise a minimal data set.

Figure 6 demonstrates the agreement between ε_{app} and ε_{mod} spectra for the parts of the plaster template differently affected by multiple scattering. For the planes and hole, differences between the measured and modeled spectra at these wavelengths were less than 0.015. For the wall the discrepancy is about 0.03. This is explained by the impossibility of exact reproduction of the actual experiment geometry with the synthetic DTM. In the synthetic DTM the angle between the wall and the lower plane was >90°, which decreased multiple-scattering effects at the wall relative to the actual measurement. Also, during the experiment the wall 'saw'' the ground due to the ~30° slope of the plaster template, which increased the apparent emissivity at the wall due to radiance reflected from the warm ground. This was not taken into account in the radiosity model. The fact that the ε (e.g. 0.85 at 8.6μm) of the surface varies greatly from both ε_{app} and ε_{mod} illustrates the importance of the cavity effect, as well as the ability of the TIR radiosity model to reproduce it in a qualitative manner.

In order to validate the heat-diffusion part of the model I used a plaster template similar to the one described above. Kinetic temperatures at different areas of the template were measured over the course of a day with a thermocouple. A synthetic DTM of the template was then generated and used as an input to the radiosity model in order to predict temperature distributions over the course of a day. The experiment was held on December 9th 2011 near town of Keeler in Owens Valley, California. Sun

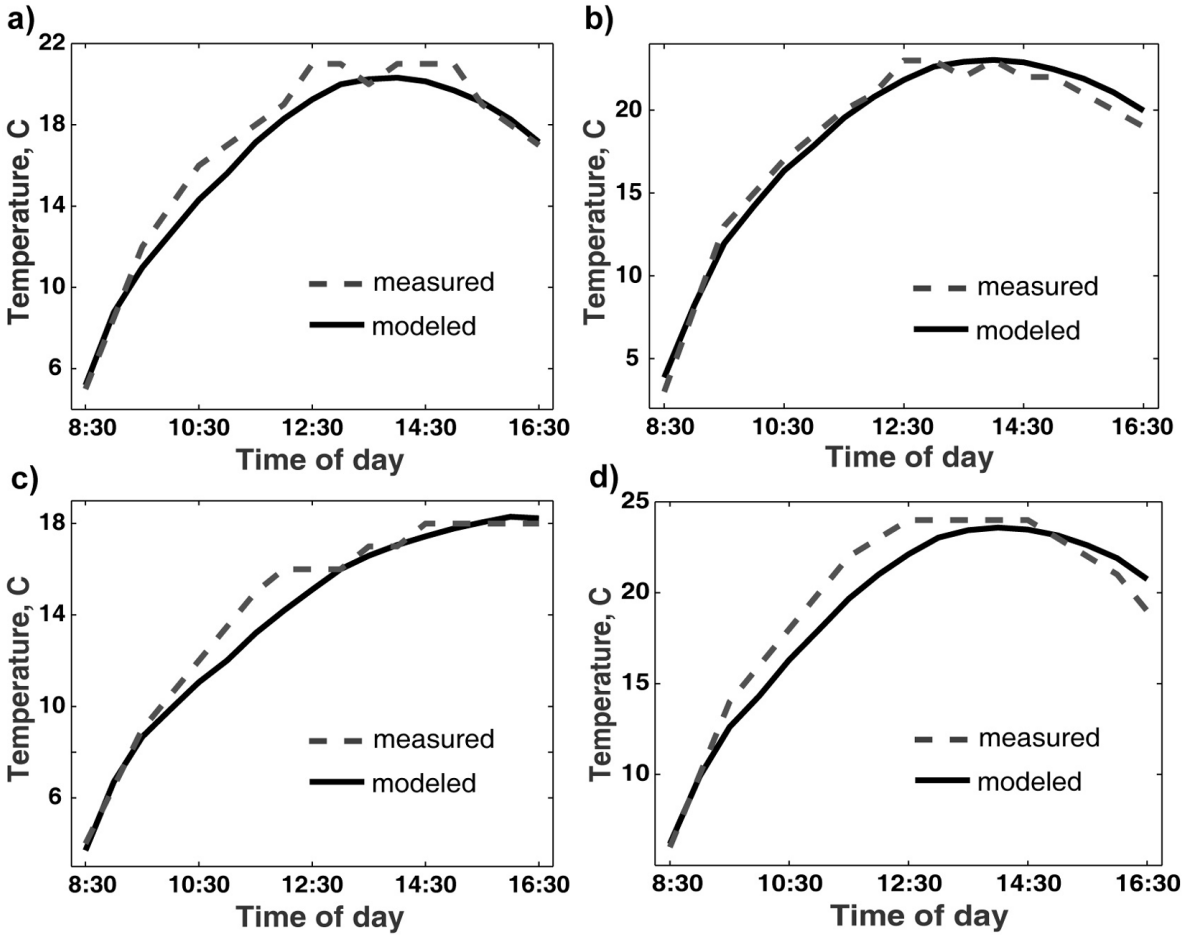

Figure 7. Heat-diffusion part of the model validation experiment results. a) Measured and modeled kinetic temperatures over the course of a day for the upper plane of the plaster template; b) for the lower plane of the plaster template; c) inside the hole located on the upper plane of the plaster template; d) for the south-facing wall of the plaster template.

elevations and azimuths were calculated for the experiment date and location and used in the model calculation, as well as typical values for thermal properties of hardened gypsum (Tesarek *et al.*, 2003). The results of the experiment are illustrated in Figure 7.

Figure 7 (a-d) compares temperatures measured in the field to those predicted by the model for different parts of the template. For the planes and hole, average differences between measured and modeled temperatures were less than 1 K. For the wall the average discrepancy was 1.12 K. The reasons that agreement for the wall is not as good as for the different areas of the template are likely the same as for the previous validation experiment and are described above. Other possible reasons for the discrepancies between measured and modeled values over the course of a day for all the areas of the template are uncertainties in thermal properties of the plaster template and instrumental errors in field temperature measurements. Despite these inexactitudes, the model demonstrated ability to closely reproduce shape and magnitude of diurnal temperature curves.

Thereby, in this chapter three validation experiments for the TIR radiosity and heat-diffusion model were described. The model demonstrated satisfactory results in all three and was able to predict diurnal kinetic and radiant temperature distributions with good accuracy. Next, Chapter 4 demonstrates examples of the model results.

CHAPTER 4: THERMAL-INFRARED RADIOSITY AND HEAT-DIFFUSION MODEL RESULTS

In this chapter, examples of the developed TIR radiosity and heat-diffusion model are demonstrated. Distributions of kinetic temperatures and radiosities were calculated over the course of a day and a night taking into account incoming solar radiation, surface geometry, thermal and spectral properties, and atmospheric conditions.

Danilina et al. (2006) showed that for the isothermal alluvial surfaces, the radiosity dispersion and the difference between actual and apparent values increase with surface roughness. Figure 8 shows that this tendency holds for anisothermal sun-heated alluvial surfaces and that ε_{mod} changes over the course of the day, as cavities change from cooler to warmer than interstices. In addition, Figure 9 demonstrates that $\Delta\varepsilon$ increases with surface roughness for bedrock and lava flow surfaces as well as for alluvial surfaces. However, results for different types of surfaces do not plot on the same trend line, which indicates that surfaces of different types should be analyzed and treated separately in future model applications.

The bedrock surface used as an example in Figures 10 and 11 was a fragment about 1 m by 1.5 m in size of a granite exposure in Owens Valley, CA. In Figure 10 a perspective view of the surface demonstrates the quality of representation of the

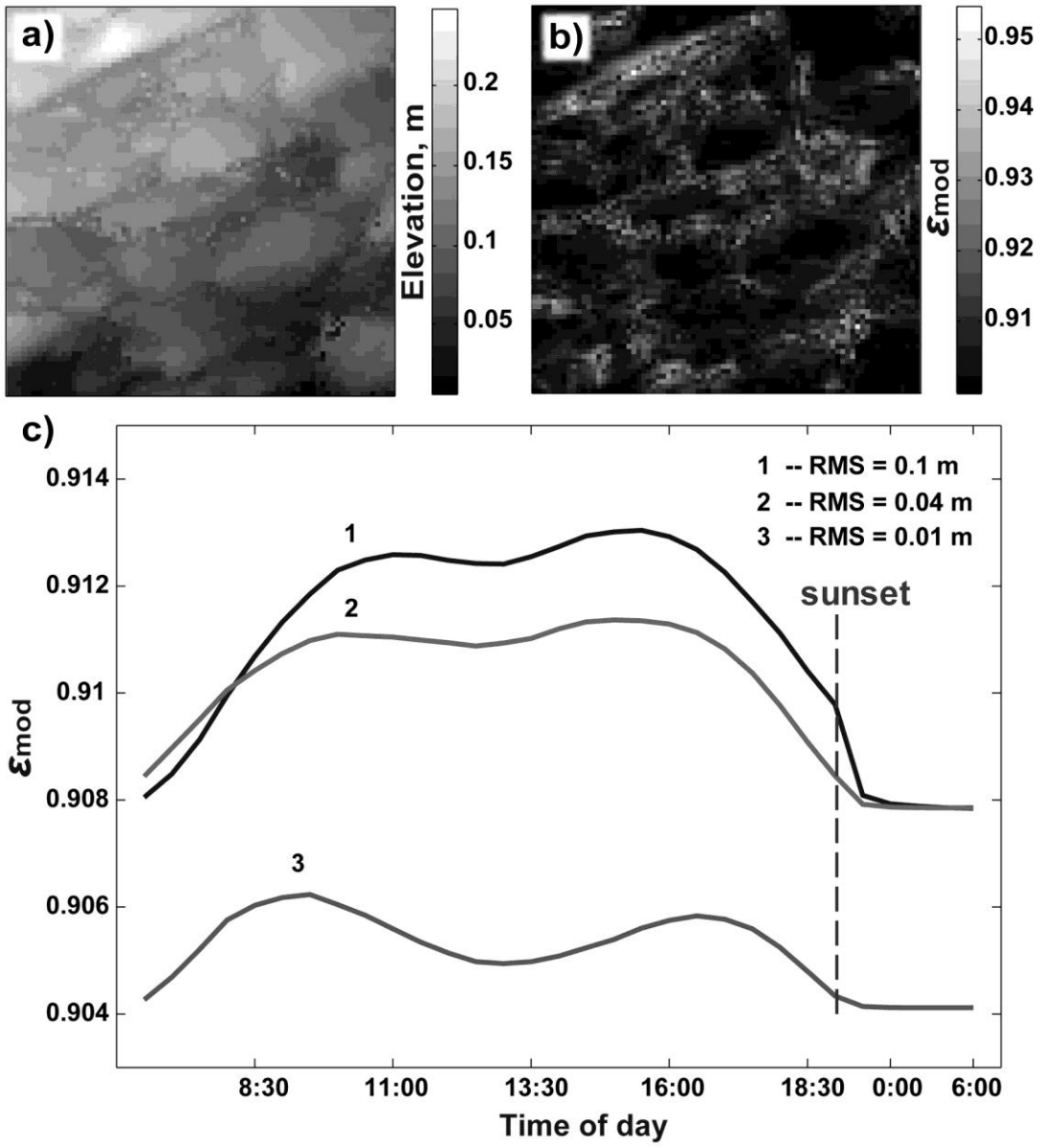

Figure 8. a) DTM for alluvial surface in Death Valley. Surface size is ~ 0.8 m by 0.8 m, pixel size is 0.01 m, RMS roughness is 0.04 m. "Noise" pixels at lower elevations are due to the DTM imperfections. b) Instantaneous ε_{mod} distribution for the same surface calculated at 14:00. ε is 0.9, ε_{mod} varies from 0.9 to ~0.95. c) ε_{mod} averaged over the course of a day for the set of alluvial surfaces of different roughnesses from Death Valley. ε was 0.9. Note different time step after sunset.

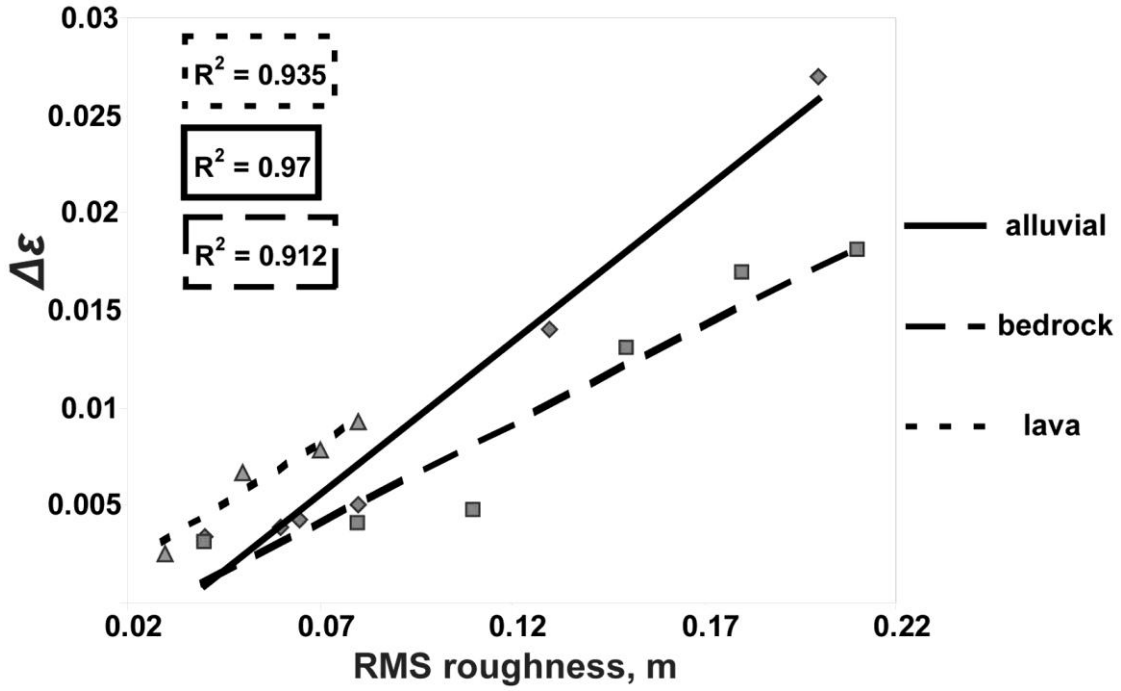

Figure 9. Effect of surface RMS on Δε in alluvial, bedrock, and lava flow surfaces. Value of ε used for the model calculations in all cases was 0.9. All surfaces were isothermal at 300K.

natural surface by a high-resolution DTM measured by the tripod-mounted LiDAR.

Predawn radiosity ranges from about 100 W/m^2 to about 145 W/m^2. This is the time when the surface is close to being isothermal, and when the main differences in radiosity are caused by multiple-scattering effects in the cavities. After dawn, sun-facing surfaces (typically tops of the rocks) are heated relative to their shadowed counterparts, and the variation of radiosity along the surface is also due to the variation in kinetic temperature. At 14:00 the radiosity range is from 140 to 280 W/m^2. Figure 10 (d) illustrates the modeled temperature over the course of a day for differently oriented facets on the surface.

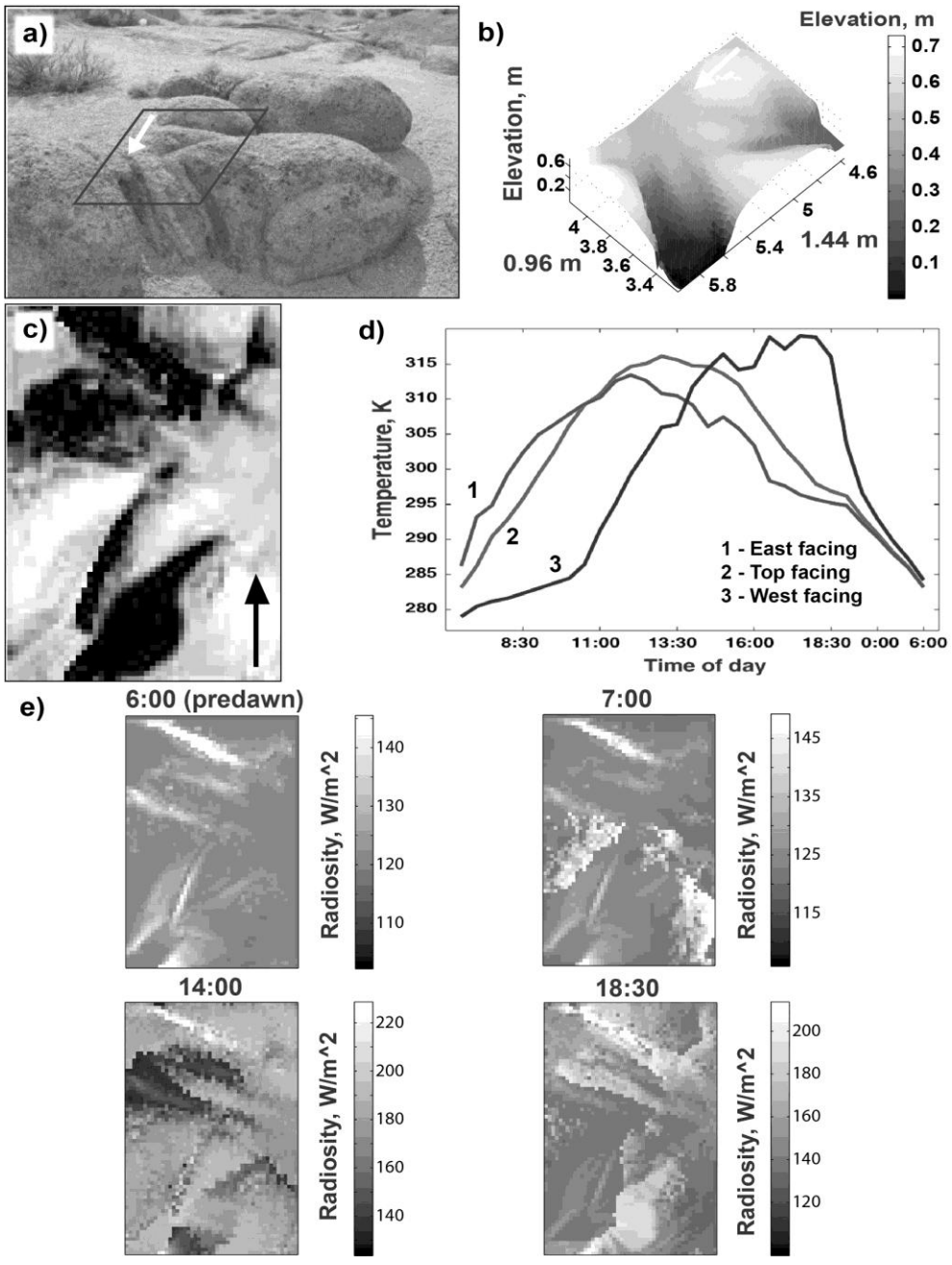

Figure 10. The radiosity model results for a granite bedrock surface from Owens Valley. Pixel size of the surface DTM is 0.02 cm, RMS roughness is 0.18 m, ε is 0.9. a) Photo of the surface. b) Perspective surface view generated with Matlab. c) Shaded relief image of the surface. The green arrows in a, b, and c indicate direction of north. d) Modeled kinetic temperature over the course of a day for differently oriented parts of the surface. Note the difference in the time step after the sunset. e) Modeled radiosity distributions at different times of day. North is up. Note the different radiosity scales for the plots.

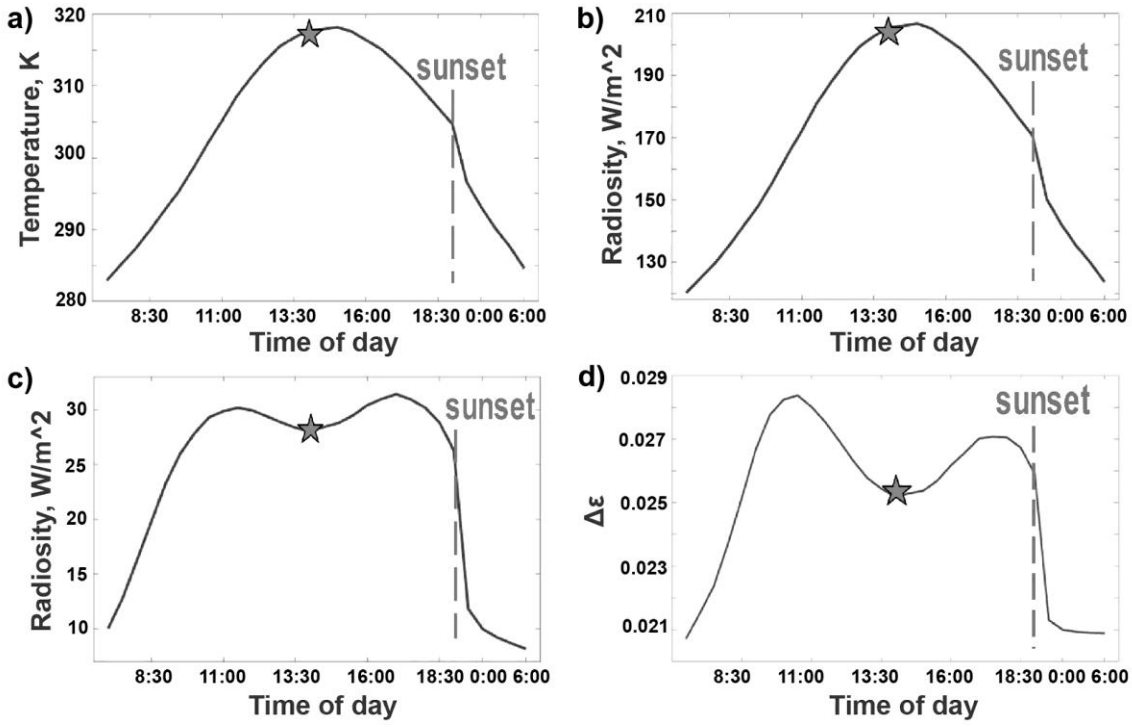

Figure 11. The radiosity model results for the same granite bedrock surface from Owens Valley, as in Figure 10. Modeled change of mean surface kinetic temperature (a), mean surface radiosity (b), radiosity RMS (c), and Δε (d) over the course of a day. The stars indicate points on the plots that correspond to 14:00 radiosity distribution (see Figure 10). Note the difference in the x-axis time step after the sunset.

Figure 11 illustrates radiosity and kinetic temperatures calculated over the course of a day and averaged over the surface, as well as root-mean-square (RMS) radiosity values and Δε values at different times. Nighttime portions of the plots have been compressed compared to the daytime ones due to the longer time step used for the modeling after the sunset.

The technique commonly used in remote sensing for emissivity retrieval is sometimes called “Planck draping.” In it, a blackbody (or graybody) radiance spectrum is computed for an upper limiting temperature and then successively lowered, “draping” the blackbody spectrum over the scene spectrum (Gillespie et al., 1998). A typical plot of emissivity over the course of a day derived with this technique starts with lower emissivity values in the morning, when rocks on ridges and elevated surfaces are heated and high-emissivity cracks are relatively cold. In the late afternoon emissivity peaks: the high spots cool off first, so the average emissivity is shifted to higher values since the cracks are favored. The experimental calculation showed that the emissivity derived from modeled radiosity data using a similar technique follows the same pattern.

However, in the example described here I used radiosities and kinetic temperatures calculated by the radiosity model to retrieve ε_{mod} over the course of a day. The plot of $\Delta\varepsilon$ shown in Figure 11 (d) does not mimic the quasi-sinusoidal behavior of mean radiosity and mean temperature plots and has two peaks instead of one peak over the course of a day. The peaks are observed in the late morning and late afternoon, when the dispersion of temperature, and therefore radiosity, is the highest. In the middle of the day the sun is high, so both tops of the rocks and

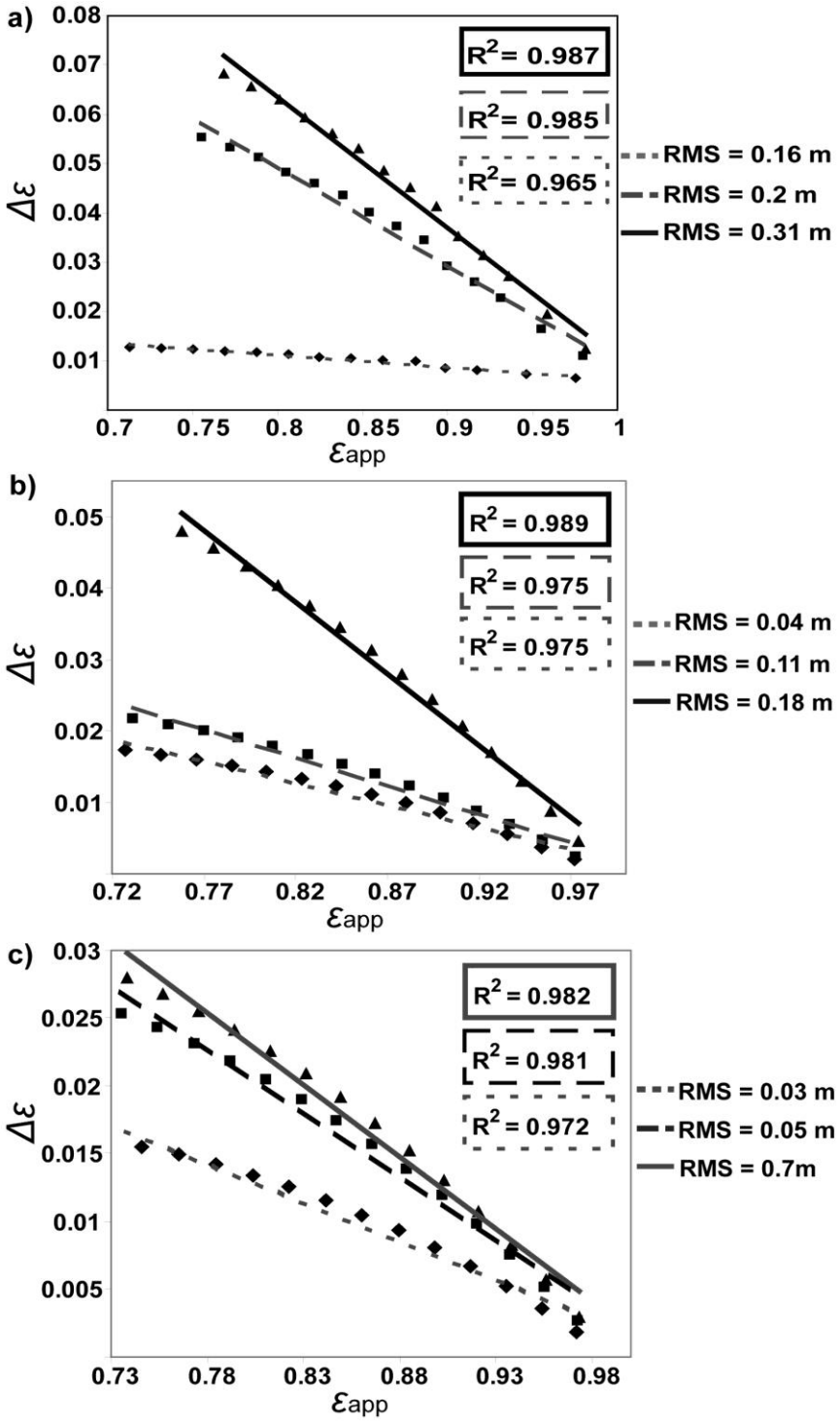

Figure 12. Generalized transfer functions for alluvial(a), bedrock(b), and lava(c) surfaces. The functions relate $\Delta\varepsilon$ to ε_{app} and were calculated using the TIR radiosity model for surfaces with different RMS roughness.

cavities get heated and rough surfaces come closer to being isothermal. At this time $\Delta\varepsilon$ drops by more than 10 %. Supposedly, the two-peaked plot better describes behavior of emissivity of natural rough surfaces over the course of a day, because the modeled kinetic temperatures I used for emissivity retrieval at each step are more accurate than estimations used in the Planck-draping technique. The model results demonstrate that the magnitude of roughness effects for TIR measurements of natural surfaces varies significantly during the course of the day

The roughness data and radiosity calculated for a gamut of surface DEMs can be related empirically. It is possible from the radiosity modeling to construct curves relating ε_{app} to ε, as in Figure 12. Modeled apparent emissivity (ε_{mod}) approximates ε_{app}. Therefore, $\Delta\varepsilon$ is applied to ε_{app} in order to compensate for the cavity effect. It is important that the radiosity calculations are individualized for the actual time and date of interest (e.g. TIR image acquisition) to account for the differential solar heating of the surface.

This chapter illustrated TIR radiosity and heat-diffusion model results. An example of a full calculated data set was given for a bedrock surface, as well as generalized transfer functions for sets of surfaces of different type, which can be used in model applications as will be demonstrated in Chapter 5.

CHAPTER 5: APPLICATIONS OF THE TIR RADIOSITY AND HEAT-DIFFUSION MODEL

The TIR radiosity and heat-diffusion model presented in this dissertation allows the estimation of multiple-scattering effects in complex natural surfaces at sub-pixel scale, as well as predicting kinetic temperature distributions for such surfaces over the course of a day. This is useful for several applications in remote sensing, planetary science, and geology.

5.1 Compensation for sub-pixel roughness effects in TIR images

The fundamental parameter measured in TIR remote sensing is spectral radiance L_S:

$$L_S(\lambda,T) = \tau(\lambda)\pi^{-1}(\varepsilon(\lambda)M_{BB}(\lambda,T) + (1 - \varepsilon(\lambda))(S^{\downarrow}(\lambda) + R(\lambda))) + S^{\uparrow}(\lambda), \quad (9)$$

where L_S ($Wm^{-2}\mu m^{-1}str^{-1}$) is the spectral radiance measured at wavelength λ and surface kinetic temperature T, τ is atmospheric transmissivity, M_{BB} ($Wm^{-2}\mu m^{-1}$) is blackbody spectral radiant exitance (defined by Planck's Law), $S^{\downarrow}$ ($Wm^{-2}\mu m^{-1}$) is downwelling spectral irradiance, R ($Wm^{-2}\mu m^{-1}$) is the spectral irradiance from neighboring surface elements, and $S^{\uparrow}$ ($Wm^{-2}\mu m^{-1}str^{-1}$) is the path spectral radiance.

Parameters τ and $S^{\uparrow}$ pertain to the path between the surface and the spectrometer, short in ground-based field experiments; $S^{\downarrow}$ is independent of spectrometer position.

In general, L_S is inverted to find T and ε_{app} after model correction for τ and $S^{\uparrow}$. Some algorithms (e.g., Gillespie *et al.* 1998) also correct for $S^{\downarrow}$, but in general R – and with it the cavity effect – is overlooked since there is no simple way to estimate it.

Neglecting to correct for R will lead to underestimation of contrast in recovered emissivity spectra (ε_{app}), regardless of the scale of the roughness elements. In his dissertation, Li (1997) showed that in the visible/near-infrared (VNIR) for resolved rough topography $(1-\varepsilon)R\pi^{-1}$ can exceed 20% of L_S. Natural surfaces tend to have lower reflectivity in TIR than in VNIR, but multiple reflection and cavity effects are significant in both spectral regions. Analysis of gamut of DTMs of natural surfaces demonstrated that at the finer, unresolved (subpixel) scales discussed in this paper this term can be as much as ~10%.

Image compensation for coarse-scale roughness uses a TIR radiosity model to calculate R(λ). As stated earlier, the model must accounts for changing illumination geometry over the course of a day, thermo-physical properties of the surface material, multiple-scattering effects, sensible heat transfer at the surface-air boundary, and downwelling sky radiation. The main driver is a DTM of the topography at the pixel scale. The problem for subpixel roughness, discussed herein, is more complex because fine-scale (cm) DTMs are commonly not available. Here I explore a possible way around this problem using remotely sensed proxies for roughness.

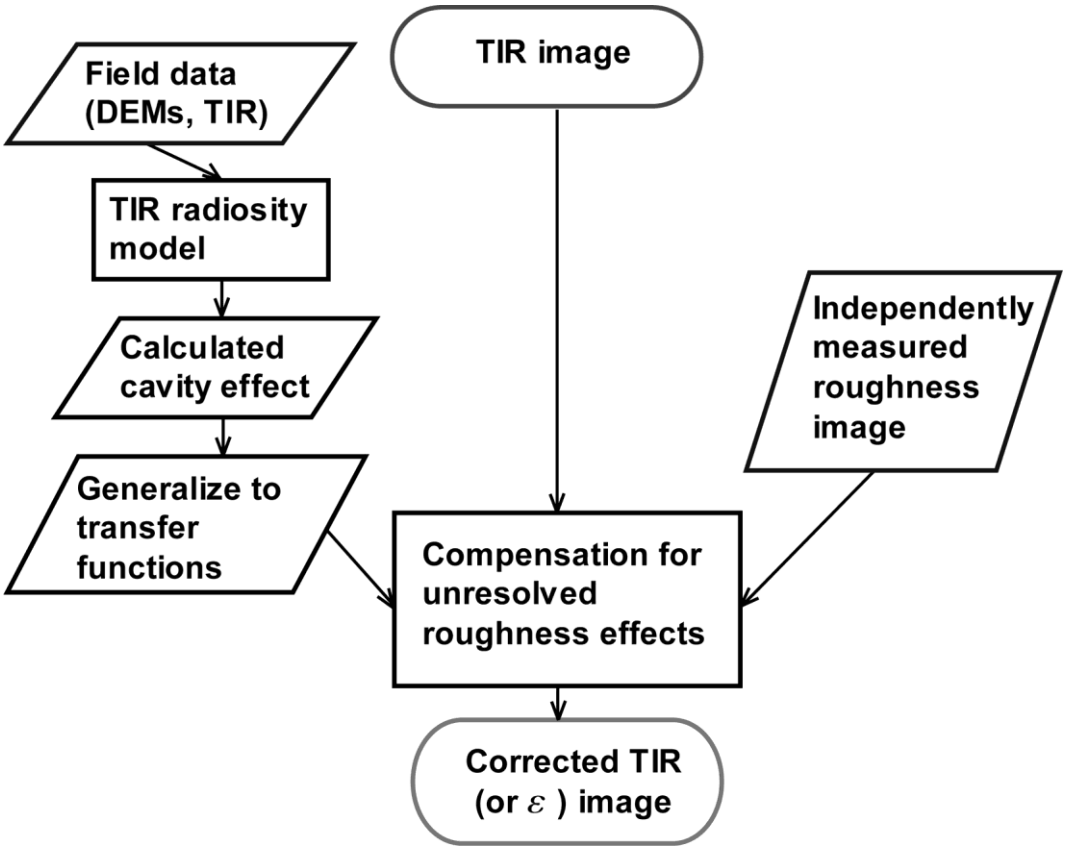

Figure 13. Flow chart illustrating approach to compensation for sub-pixel roughness effects in TIR images.

The image-processing model uses as input the TIR apparent emissivity image to be corrected and a co-registered image of subpixel roughness. In addition, curves or transfer functions are required for relating the contribution of cavity radiation from landscape elements of different roughnesses, calculated for the time of image acquisition using a TIR radiosity model. The processing procedure uses the roughness image to predict the amount of cavity radiation, and then to unmix it from the apparent emissivity using standard linear mixing models that have been developed

and applied both to the spectral radiance data and to the emissivites. A flow chart illustrating the approach used here is shown in Figure 13.

Estimating $R(\lambda)$ requires determining unresolved roughness, pixel by pixel. Two approaches have been used: inversion of models relating backscatter to roughness in synthetic aperture RADAR (SAR) images, and inversion of models relating reflectance lowering caused by unresolved shadows to roughness (Weeks *et al.* 1996; Mushkin and Gillespie 2005). The SAR approach requires accounting for soil moisture; the optical approach requires separating the darkening effects of shadowing. In either, it is necessary to calibrate the image-derived parameters to some conventional measure of surface roughness from which $R(\lambda)$ can be estimated.

Mushkin and Gillespie (2005) related ASTER nadir- and aft-looking (27.6°) near-infrared (NIR) brightness ratios (two-look method) to surface topographic RMS independently measured at cm−m spatial scales. For calibration, the RMS roughness is calculated from fine-scale DEMs measured at test sites in the field.

I compared root mean squared **(**RMS**)** roughness values for Trail Canyon fan, Death Valley, California, USA, derived using the two-look method to the similar values derived from RADAR backscatter data (Greeley *et al.* 1995), using region of interest statistics for corresponding areas. The values demonstrated good subjective agreement (Figure 14), but the two-look results showed smaller levels of variability within samples. This is explained by the fact that ASTER NIR data do not suffer from

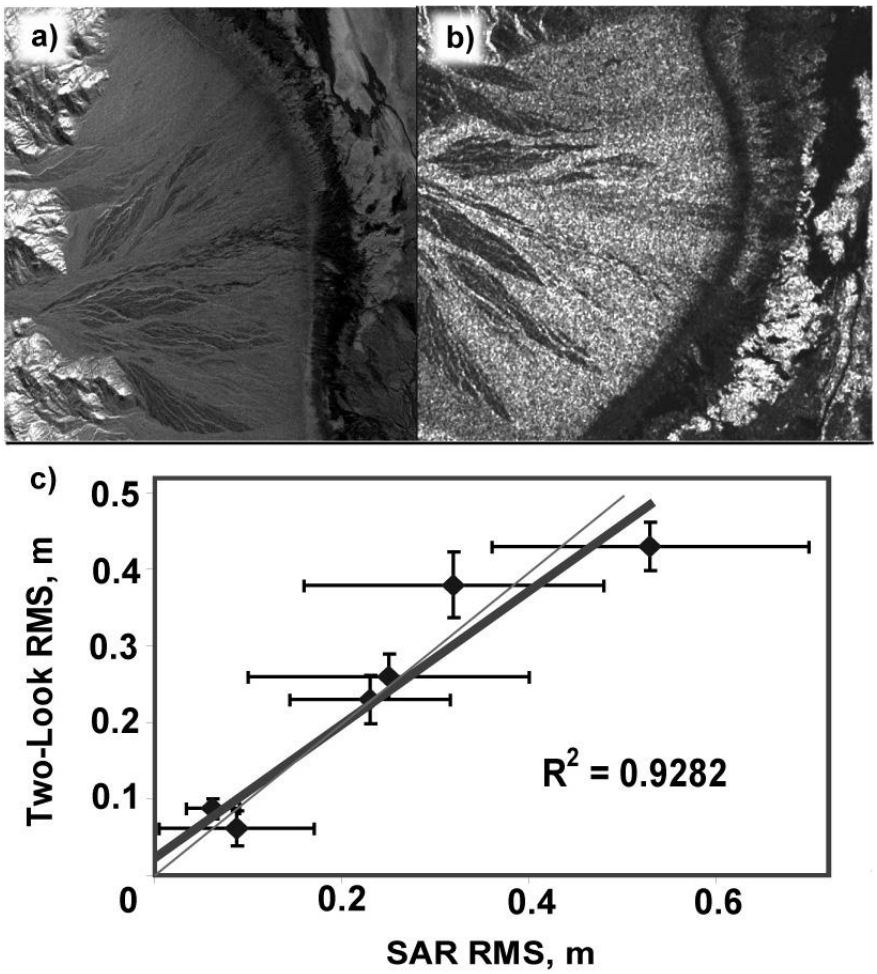

Figure 14. a) RMS roughness image derived using two-look method (Mushkin and Gillespie 2005) for Trail Canyon fan, Death Valley, CA, USA. b) RMS roughness image derived from RADAR image (SIR-C, C band, HV polarization) of the same area. c) Correlation between mean RMS roughness for various regions of interest in the area derived using two different methods. Bold line illustrates linear trend. Thinner line illustrates actual diagonal. The error bars represent standard deviation within the regions of interest.

'speckle' noise as much as RADAR data do. This is one of the advantages of the two-look method.

The two-look approach to measuring roughness has also been used to help select the Phoenix landing site on Mars (Arvidson *et al.,* 2008). In this case the stereo images could be calibrated by field measurements of roughness at Rover sites, and compared to boulder counts in high-resolution HiRISE images of parts of the landing-site candidate areas.

As shown in Chapter 4, $\Delta\varepsilon$ (Figure 11(*d*)), does not mimic the quasi-sinusoidal behavior of mean radiosity and mean temperature plots. The largest differences are registered in the late morning and late afternoon. In the middle of the day when the sun is high $\Delta\varepsilon$ drops by more than 10%. This demonstrates the importance of using a TIR radiosity model to predict roughness effects for natural surfaces for any given time (e.g. the time of a satellite overflight). Chapter 4 also demonstrates examples of ε_{app} to ε transfer functions for natural surfaces of different types (Figure 12).

In method proposed here, once R has been estimated for a roughness image such as Figure 15(*a*), it is straightforward to subtract it from the measured L_S, after atmospheric compensation. The resulting difference is the "ground-emitted spectral radiance," and standard methods can be used to calculate ε from it. It is also possible to use shortcuts, for example if curves have been calculated that relate ε_{app} to ε directly (Figure 12). Again, the roughness image must be used to select the curve for the appropriate roughness, pixel by pixel across the image.

Good quality of registration between the roughness image and the emissivity image to be compensated is essential. For ASTER, however, such quality is hard to

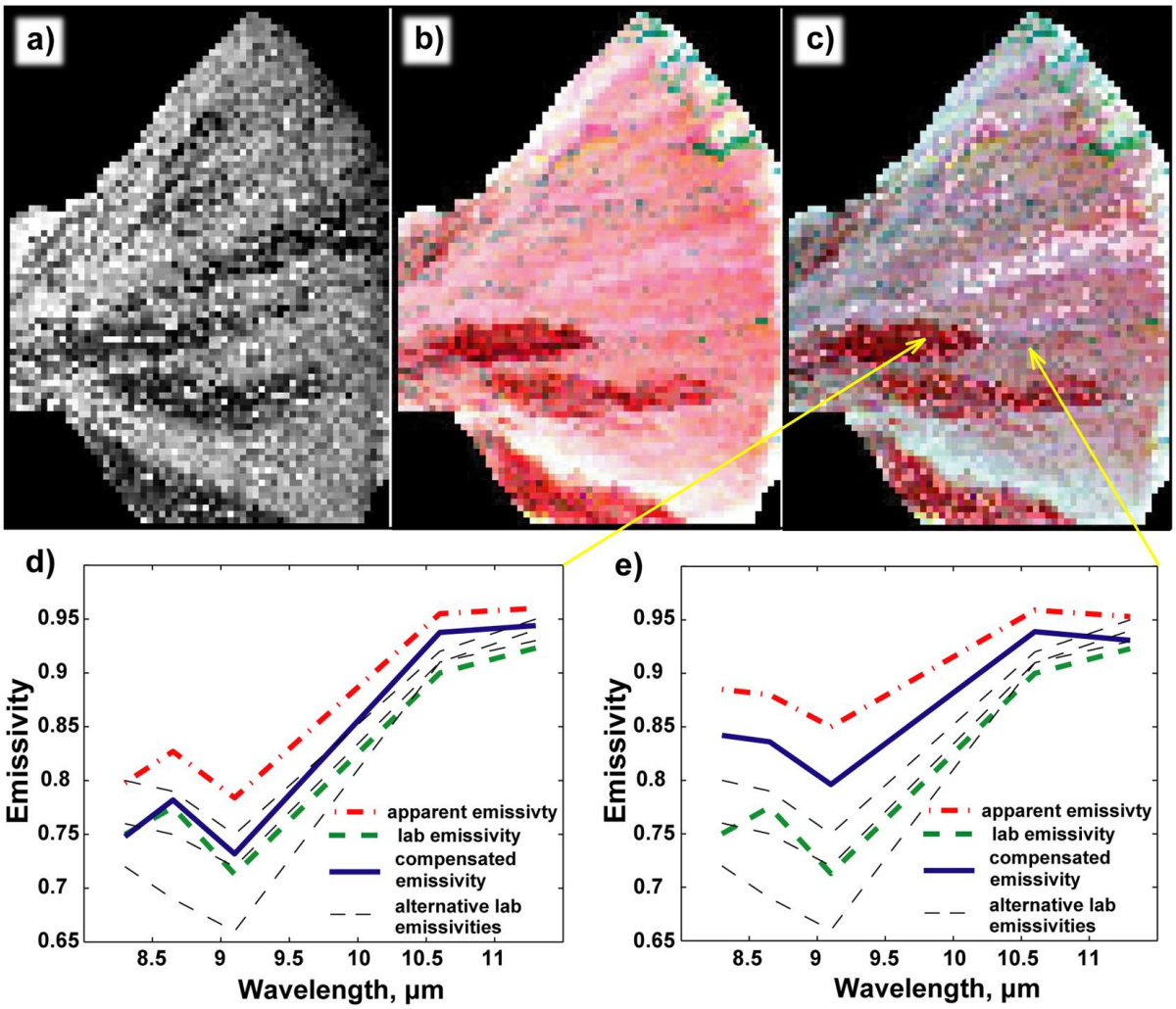

Figure 15. a) ASTER nadir- and aft-looking NIR ratio image for Trail Canyon fan calibrated to RMS roughness measured at test sites (two-look method). Black–white range runs from RMS = 0.14 to 0.4. b) ASTER emissivity image for the same region (RGB = 10.6 µm, 9.1 µm, 8.65 µm). c) Emissivity image compensated for cavity effect (RGB = 10.6 µm, 9.1 µm, 8.65 µm). d) Cavity compensation for QG_2 pixel (RMS = 0.2 m). e) Cavity compensation for QG_3 pixel (RMS = 0.37 m). Yellow arrows indicate location in the compensated image of the pixels used in examples in Figure 15(d,e).

achieve due to differences in spatial resolution between NIR bands used for sub-pixel roughness estimation and TIR bands used for emissivity retrieval.

Figure 15(*c*) shows an ASTER emissivity image of Death Valley acquired on April 7th 2000, compensated for the cavity effect using the transfer-function approach described above. The image was sub-setted to show only the Trail Canyon fan. The procedure is implemented automatically, pixel by pixel. On the basis of elevation RMS values, the appropriate transfer function is chosen for each pixel from the set defined for alluvial surfaces beforehand using the TIR radiosity model (Figure 12(a)).

Figure 15(*d*) demonstrates an example of an emissivity spectrum of a pixel of a smooth, low-roughness (RMS = 0.2 m) surface from the Trail Canyon fan. This surface, covered by "desert pavement" of the geological unit QG_2 (Hunt and Maybe 1966), appears dark in Figure 15(*a*). The spectrum was sampled from the ASTER image after compensation for the cavity effect (Figure 15(*b*,*c*)). In the compensation procedure the appropriate transfer function estimated with TIR radiosity model (Figure 12(a)) was used. The compensation increased spectral contrast 24%, from 0.17 for the image spectrum to 0.21 for the compensated spectrum.

Similarly, Figure 15(*e*) is an example of cavity-effect compensation for a pixel representing a rougher surface with RMS = 0.37 m (geological unit QG_3: Hunt and Maybe 1966). Spectral contrast was increased 27%, from 0.11 for the image spectrum to 0.15 for the compensated spectrum.

I have not measured emissivity spectra in the field for the area of interest, to which I could compare the compensated spectra. Therefore, I used laboratory spectra of granite to approximate the varnished rocks (a mixture of quartzite, schist, and

dolomite) of Trail Canyon fan. The similarity arises because of opaline silica in the varnish, and quartz and feldspar in the granite spectrum, and breaks down under high spectral resolution. In Figure 15 (*d,e*) green dashed line shows laboratory spectra of granite with the spectral shape close to that measured by ASTER for QG_3 surface. All the thinner dashed black lines show alternative library spectra for granite.

In conclusion, a protocol for compensating remotely sensed emissivity images for the effects of surface roughness is developed. The inputs to the model are TIR spectral radiance images (or apparent temperature and emissivity images), a co-registered image of surface roughness, and transfer functions generated by a TIR radiosity model. The transfer functions relate the decrease in ε_{app} compared to ε for a given roughness. Further analysis of gamut of natural surfaces DTMs is necessary in order to determine types of surfaces that can be treated together using a single roughness calibration and set of transfer functions, as well as the types of surfaces for which the compensation approach discussed here is suitable.

5.2 3-D modeling of icy landscape evolution on Callisto

Erosion is a major landscape-shaping process on the Galilean satellites, along with tectonism, cryovolcanism, and impact cratering, of which an understanding is critical to their geologic characterizations. The most common positive relief landforms on Callisto are knobs, which appear to be remnants of crater rims (Figure 16), central peaks, palimpsests and ejecta deposits (Moore *et al.*, 1999, 2004; Basilevsky, 2002).

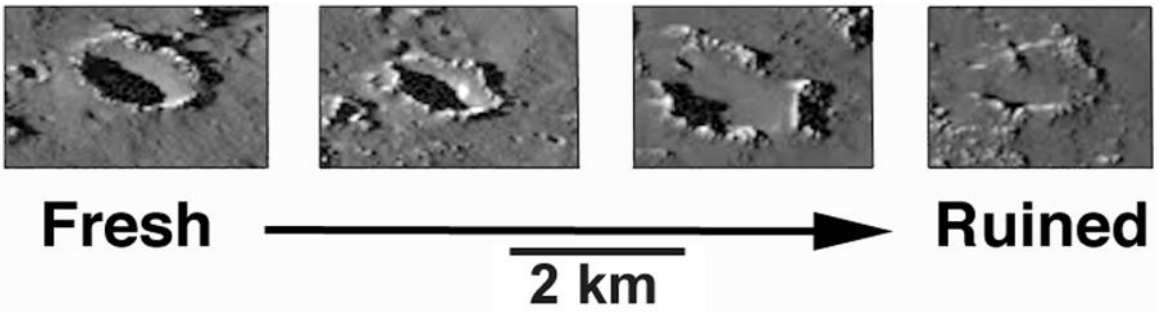

Figure 16. High resolution Galileo images showing impact craters on Callisto in various states of erosion transforming them ultimately into knobs surrounded by a largely infilled depressions (Moore et al., 2004).

The loss of a volatile rock-forming matrix or cement mixed with a dark refractory fine-grained material is attributed for the degradation of pristine landforms into knobs (e.g., Moore *et al*., 1999, 2004; Greeley *et al*., 2000; Chuang and Greeley, 2000; Basilevsky, 2002).

In order to test hypotheses related to these landform and albedo patterns, Wood *et al.* (2010) developed a 3-D thermal model. Model simulations of icy satellite landform erosion and volatile redistribution are guided and constrained by iteratively comparing model results with the general statistics of erosional landform classes derived from DTMs produced using Galileo data. In some cases, DTMs of pristine landforms (e.g. fresh craters, fault blocks) are used as the "initial conditions" in model runs. The model includes the following coupled processes: (a) sublimation and re-condensation of surface volatiles; (b) subsurface heat conduction; (c) direct solar heating and radiative cooling; (d) indirect solar and thermal radiation from other

surfaces (reflected and emitted); (e) shadowing by topography; (f) subsurface sublimation/condensation and vapor diffusion; (g) development of a "sublimation lag" of non-volatile material; and (h) disaggregation and downward sloughing of surficial material. For items (d) and (e) the radiosity model described in this dissertation was used. In order to accommodate both TIR and visible (solar) radiosity and irradiance the model was modified according to Lagerros *et al.* (1997).

5.3 Solar stresses and fractures in exposed rocks

In their study, McFadden *et al.* (2005) observed the preferred north-south and near vertical orientations of many rock-surface cracks in boulders and cobbles. They hypothesized this phenomenon to be fundamentally related to thermal stresses that arise daily from non-uniform solar heating. It was proposed that this process, alone or together with other processes, plays a key role in the physical weathering of rocks exposed to the sun. Once cracks form, they extend, widen, and ultimately may break down the entire clast (Figure 17(a)), either through the formation of later generations of such cracks or by facilitating salt-weathering or other physical weathering mechanisms.

In order to model this process, it is important to accurately estimate surface and internal temperatures of rocks over the course of a day, as well as at a larger time scale. The model described in this dissertation proved to be a good tool for reproducing shape and magnitude of diurnal temperature curves, as it takes into

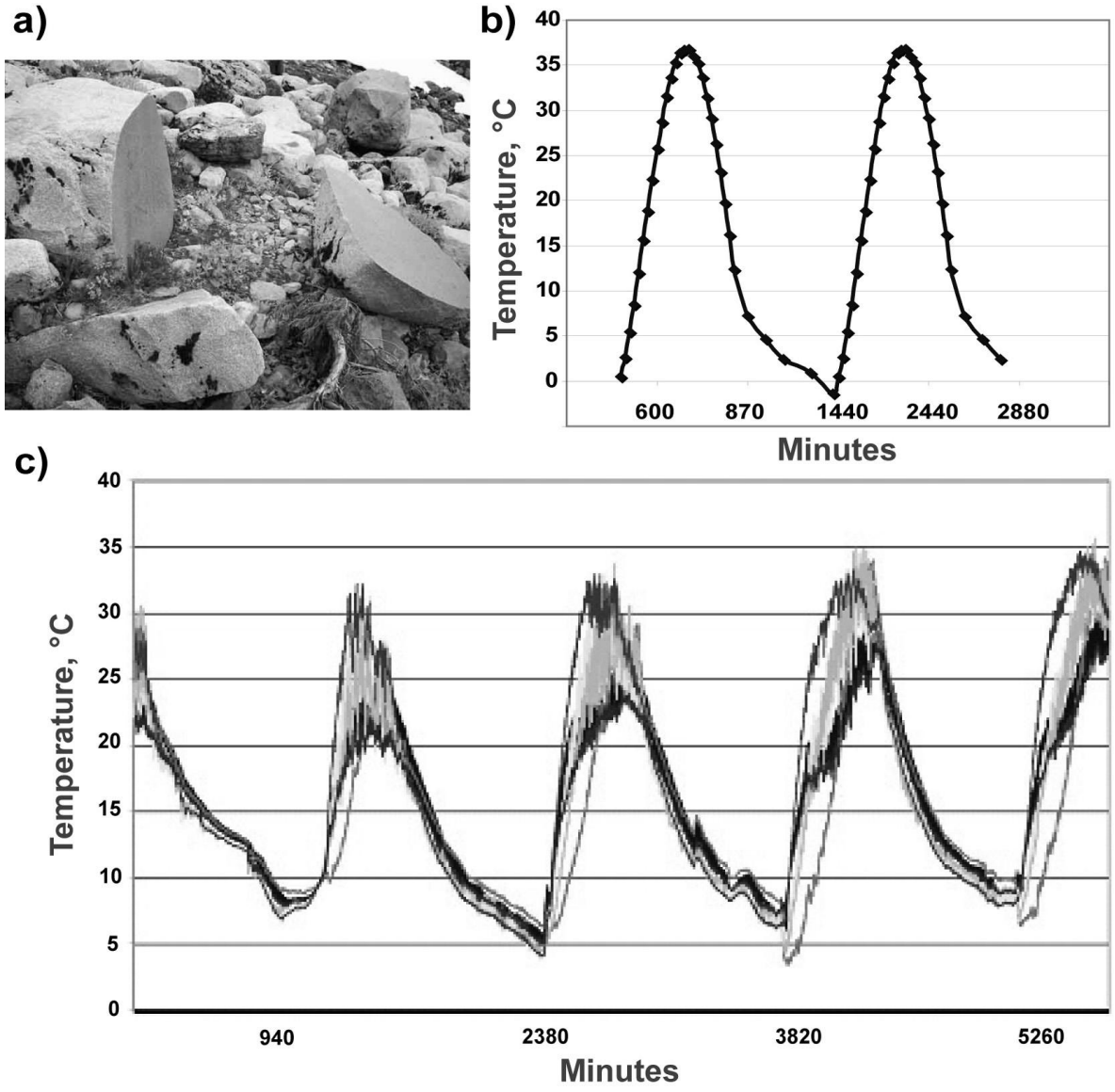

Figure 17. a) Clean fracture splitting boulder (~0.5m in diameter) in Cascade Mountains (courtesy of Prof. B. Hallet). b) Mean surface temperature calculated by the model for a rock, similar in size and shape to the one used for Arkaroola experiment. Parameters used in the model were characteristic for the location and time of the experiment. c) Results of thermocouple monitoring of rock temperatures in one-minute intervals in Arkaroola, Australia in August 2004. Different curves are for differently oriented facets on the rock surface (courtesy of Prof. B. Hallet).

account effects of changing illumination geometry, thermo-physical properties of the surface material, multiple-scattering effects, sensible heat transfer at the surface-air boundary, and downwelling sky radiation. Hence, it has been used as a part of a modeling effort in order to simulate thermal stresses and fracture propagation due to daily heating of a partly buried clast. Figure 17 demonstrates the similarity of diurnal curves estimated by the model described here to ones measured with a thermocouple in Arkaroola, Australia in August 2004.

In this chapter possible applications of the TIR radiosity and heat-diffusion model were discussed. The main and most obvious application is compensation for sub-pixel roughness effects in TIR images. In addition, the model is useful for 3-D modeling of the evolution of icy landscapes on the Gallilean and Saturnian satellites and kinetic temperature predictions for solar stress and fracture in exposed rocks.

CHAPTER 6: **SUMMARY**

Temperature/emissivity estimation from remotely measured radiances generally assumes that scene elements represented by pixels in fact have a single emissivity spectrum and are isothermal. Thus, estimated temperatures and emissivities are the effective values that would be found if these simplified assumptions were met. In reality, the physical scene is neither homogeneous nor isothermal, and the effective values are not strictly representative of it. How much in error are they? The objective of this research was developing an effective and comprehensive model in order to estimate this.

Here I have demonstrated that there is significant variation of radiant and kinetic temperatures over natural complex surfaces due to the combined effect of the reflection of thermal radiation between adjacent scene elements, and both heat-conduction effects and emitted radiation determined by the kinetic temperature. The magnitude of roughness effects for TIR measurements of natural surfaces varies significantly during the course of the day. The distribution of radiant temperatures depends on the roughness and type of surface. Thus it would be difficult to predict this distribution with simple statistical models that do not take into account the organization of the surface roughness elements. The apparent emissivity also varies

because of the cavity effect: Since reflection and emission are complementary, for very rough surfaces the apparent emissivity approaches unity.

In order to predict kinetic and radiant temperatures distributions over the course of a day, I developed a 3-D radiosity model adapted for TIR, and coupled it with a 1-D (downward) heat-diffusion model. The model takes into account incoming solar radiation (changing sun position), surface geometry, multiple scattering effects, thermo-physical and spectral properties of the surface material and atmospheric conditions. Performance of the model was verified using an analytical solution to the simple case of radiation between single surface element and a large finite wall, parallel to the element. I found errors that never exceeded a fraction of percent. In validation experiments the discrepancies between modeled and measured emissivity spectra were less than 1.5%. In validation of the heat diffusion part of the model the average differences between measured and modelled kinetic temperatures over the course of a day were less than 1K.

I also present an example of the radiosity model results for the set of natural alluvial surfaces and granite outcrops from the Mojave Desert (CA), as well as some lava flow surfaces from Hawaii. These illustrate the need to consider roughness effects in order to improve the accuracy of temperature/emissivity separation algorithms. The thermal radiosity model appears to be ready to predict spectral emissivities and radiant temperatures provided that representative high-resolution DTMs are available. This will facilitate comparison of lower-resolution ‘effective’

values recovered in airborne or spaceborne remote sensing to the distribution of actual values on the spatially integrated surface.

Here I concentrated on the case of homogeneous surfaces. However, the model can also accommodate non-homogeneous surfaces with facets with different spectral signatures in the TIR spectrum.

In Chapter 5 I discussed possible applications of the developed model, including 3-D modeling of icy landscapes evolution on the Gallilean and Saturnian satellites and kinetic temperature predictions for solar stress and fracture in exposed rocks. However, the straightforward and most important application of the model is compensation for sub-pixel roughness effects in TIR images.

I presented a protocol for compensating remotely sensed emissivity images for the effects of surface roughness. The inputs to the model are TIR spectral radiance images (or apparent temperature and emissivity images), a co-registered image of surface roughness, and transfer functions generated by a TIR radiosity model. The transfer functions relate the decrease in ε_{app} compared to ε for a given roughness.

It is necessary currently to calibrate the remotely sensed roughness proxy to standard measures of roughness before they can be used in compensation. Furthermore, separate calibration is required for slopes >5° and for all view and illumination angles. This current requirement for calibration of the two-look ratio images with field measurements is a difficulty in using the approach, but in the future this difficulty may be lessened by using pre-calculated transfer functions compiled in

a library and selected from DEM slopes and aspects and from image classification for surface type.

In the example shown in Chapter 5, elevation RMS was used as parameterized roughness because calibrated data were already available for Trail Canyon (Mushkin and Gillespie 2005). Other parameterizations of unresolved roughness are possible (Weeks et al. 1996) and may be used alone or in combination with elevation RMS for better description of natural surfaces of different types.

A focus of future work should be the identification of types of surfaces that can be treated together using a single roughness calibration and set of transfer functions, as well as the types of surfaces for which the compensation approach discussed here is suitable. For example, I showed that it works effectively for gravels, whereas it may not be worthwhile correcting data for forest canopies since the emissivity is high even for single leaves, and only gets closer to unity for canopies. Consequently, the correction is likely to be small relative to measurement precision. Resolving these and related issues requires further analysis of DTMs of natural surfaces in order to find more regularities between roughness parameters and cavity effect.

It seems to be necessary to amass and assimilate more experience with the developed TIR radiosity and heat-diffusion model in order to explore possibilities of its application further. In spite of this, it can be affirmed that it is a useful tool for estimation of sub-pixel distributions of kinetic and radiant temperatures, as well as spectral emissivities, over the course of a day.

BIBLIOGRAPHY

Arvidson, R., Adams, D., Bonfiglio, G., Christensen, P., Cull, S., Golombek, M., Guinn, J., Guinness, E., Heet, T., Kirk, R., Knudson, A., Malin, M., Mellon, M., McEwen, A., Mushkin, A., Parker, T., Seelos IV, F., Seelos, K., Smith, P., Spencer, D., Stein, T., and Tamppari, L., (2008). Mars Exploration Program 2007: Phoenix landing site selection and characteristics. *Journal of Geophysical Research*, **113**, E00A03, doi:10.1029/2007JE003021.

Balick, L.K., Hutchinson, B.A. (1986). Directional thermal infrared exitence distributions from a leafless deciduous forest. *IEEE Trans. Geosci. Rem. Sens*. GE-24, 693–698.

Bandfield, J.L. (2009). Effects of surface roughness and graybody emissivity on martian thermal infrared spectra, *Icarus*, 202, 10.1016/j.icarus.2009.03.031.

Basilevsky, A.T.,(2002). Morphology of Callisto knobs from photogeologic analysis of Galileo SSI Images taken at Orbit C21. *Lunar and Planetary Science Conf.* XXXIII, 89–90, Lunar and Planetary Institute, Houston (CD-ROM).

Brutsaert, W. (1975). On a derivable formula for long-wave radiation from clear skies. *Water Resources Research* 11, 742–744.

Chuang, F.C. and Greeley, R. (2000). Large mass movements on Callisto. *Journal of Geophysical Research,* 105, 20227-20244.

Danilina, I., Mushkin, A., Gillespie, A. R., O'Neal, M. A., Abbott, E. A., Pietro, L. S., & Balick, L. K. (2006). Roughness effects on sub-pixel radiative temperature dispersion in a kinetically isothermal surface. *Abstract Book, Conference on Recent Advances in Quantitative Remote Sensing II (RAQRS II),* University of Valencia, Spain, Sept. 25–29, p. 31.

Dozier, J. (1981). A method for satellite identification of surface temperature fields of subpixel resolution. *Remote Sensing of Environment* 11, 221–229, doi:10.1016/0034-4257(81)90021-3.

Gillespie, A. R. (1987). Lithologic mapping of silicate rocks using TIMS data. *Proceedings of the Workshop on Thermal Infrared Multispectral Scanner*, Jet Propulsion Laboratory Publication 36–38, Pasadena, CA, 29–44.

Gillespie, A. R. (1992). Spectral mixture analysis of multispectral thermal infrared images. *Remote Sensing of Environment* 42, 137–145.

Gillespie, A. R., Cothern, J. S., Alley, R.,. & Kahle, A. (1998). In-scene atmospheric characterization and compensation in hyperspectral thermal infrared images, *Proceedings of the 7th Jet Propulsion Laboratory Airborne Earth Science Workshop*, Pasadena, CA, 21–24.

Gillespie, A. R., Cothern, J. S., Matsunaga, T., Rokugawa, S., & Hook, S. J. (1998). Temperature and emissivity separation from Advanced Spaceborne Thermal Emission and Reflection Radiometer (ASTER) images. *Institute of Electrical and Electronics Engineers (IEEE) Transactions on Geoscience and Remote Sensin*g 36, 1113–1126.

Gillespie, A. R., Matsunaga, T., Rokugawa, S., and Hook, S. J., (1998). Temperature and Emissivity Separation from Advanced Spaceborne Thermal Emission and

Reflection Radiometer (ASTER) Images. *Institute of Electrical and Electronics Engineers (IEEE) Transactions on Geoscience and Remote Sensing*, **36**, pp. 1113–1126.

Goral, C., Torrance, K., Greenberg, D., & Battaile, B. (1984). Modeling the interaction of light between diffuse surfaces. *Computer Graphics* 18, 213–222.

Greeley, R., Blumberg, D. G., Dobrovolskis, A. R., Gaddis, L. R., Iversen, J. D., Lancaster, N., Rasmussen, K. R., Saunders, R. S., Wall, S. D., and White, B., (1995). Potential Transport of Windblown sand: Influence of Surface Roughness and Assessment with Radar. *Desert Aeolian Processes*, ed. V. Tchakerian, Chapman and Hall, pp. 75–99.

Gustafson, W. T., Handcock, R. N., Gillespie, A. R., & Tonooka, H. (2003). An image-sharpening method to recover stream temperatures from ASTER Images. *Proceedings of the International Society for Optical Engineering (SPIE) Workshop: Remote Sensing for Environmental Monitoring, GIS Applications, and Geology II*, Vol. 4886, Crete, Greece, Sept. 23–27, p 72–83, doi:10.1117/12.462325.

Hunt, C. B., and Maybe, M. R., 1966, Stratigraphy and Structure, Death Valley, California. *U.S. Geological Survey Professional Paper* 494–A.

Jiménez-Muñoz, J. C, Sobrino, J. A., Gillespie, A., Sabol, D., & Gustafson, W. (2006). Improved land surface emissivities over agricultural areas using ASTER NDVI. *Remote Sensing of Environment* 103, 474–487.

Lagerros, J. S. V. (1997). Thermal physics of asteroids III. Irregular shapes and albedo variegations. *Astronomy and Astrophysics*, 325, 1226–1236.

Li, W.-H. (1997). Significance of multiple scattering in remotely sensed images of natural surfaces. PhD dissertation, University of Washington, Seattle, 11–15.

McCabe, M.F., Balick, L.K., Theiler, J., Gillespie, A.R., Mushkin, A. (2008). Linear mixing in thermal infrared temperature retrieval. *International Journal of Remote Sensing*. 29, 5047–5061.

McFadden, L.D., M.C. Eppes, AR Gillespie and B. Hallet (2005), Physical weathering in arid landscapes due to diurnal variation in the direction of solar heating, *Geol. Soc. Am. Bull.*, 117, 161–173, doi:10.1130/ B25508.1.

Moore, J. M., Asphaug, E., Morrison, D., Spencer, J. R., Chapman, C. R., Bierhaus, B., Sullivan, R. J., Chuang, F. C., Klemaszewski, J. E., Greeley, R., Bender, K. C., Geissler, P. E., Helfenstein, P., Pilcher, C. B. (1999). Mass movement and landform degradation on the icy Galilean satellites: Results of the Galileo nominal mission, *Icarus* 140, 294–312.

Moore, J.M., Chapman C. R., Bierhaus E. B. *et al*. (2004). Callisto. In *Jupiter*, Bagenal, F., Dowling, T. and McKinnon, W. (Eds.), pp. 397-426. Cambridge Univ. Press, Cambridge, UK.

Mushkin, A., and Gillespie, A. R. (2005). Estimating sub-pixel surface roughness using remotely sensed stereoscopic data. *Remote Sensing of Environment,* **99**, pp. 75–83.

Pieri, D. S., Glaze, L. S., & Abrams M. J. (1990). Thermal radiance observations of an active lava flow during the June 1984 eruption of Mount Etna. *Geology* 18 (10), 1018–1022.

Ramsey, M. S., & Christensen, P. R. (1992). The Linear "Un-Mixing" of Laboratory Thermal Infrared Spectra: Implications for the Thermal Emission Spectrometer (TES) Experiment, Mars Observer. *Abstracts of the Lunar and Planetary Science Conference* 23, 1127.

Ramsey, M. S., & Christensen, P. R. (1998). Mineral abundance determination: Quantitative deconvolution of thermal emission spectra. *Journal of Geophysical Research* 103 (B1), 577–596.

Smith, J.A., Chauhan, N.S., Schmugge, T.J., Ballard Jr, J.R. (1997). Remote sensing of land surface temperature: The directional viewing effect. *IEEE Trans. Geosci. Rem. Sens*. 35, 972–974.

Sobrino, J. A., & Li, Z.-L. (2002). Land surface temperature and emissivity retrieval from remote sensing data. *Recent Research Developments in Geophysics* 4, 21–44.

Sparrow, E. (1963). A new and simple formulation for radiative angle factors. *American Society of Mechanical Engineers (ASME) Journal of Heat Transfer* 85, 81–88.

Sparrow, E., & Cess, R. (1978). *Radiation Heat Transfer*. Hemisphere Publishing, Washington D.C., 366.

Tesárek P., Černý R., Drchalová J., Rovnaníková P. (2003) Thermal and Hygric Properties of Gypsum: Reference Measurements, *Thermophysics 2003,* Bratislava: Slovak Academy of Sciences, 52–57.

Wan, Z., & Li, Z.-L. (1997). A physics-based algorithm of retrieving land-surface emissivity and temperature from EOS/MODIS data. *Institute of Electrical and Electronics Engineers (IEEE) Transactions on Geoscience and Remote Sensing* 36, 980–996.

Weeks, R. J., Smith, M. O., Pak, K., Li, W. H., Gillespie, A. R., & Gustafson, W. (1996). Surface roughness, radar backscatter and VNIR reflectance in Death Valley, California. *Journal of Geophysical Research* 101, 23077–23090.

Wood, S. E., Ivarson, K. L., Danilina, I., Griffiths, S. D., Moore, J. M., Howard, A. D., Schenk, P. M. (2010). 3-D Topographic thermal and radiative modeling of Ice Stability and Migration on Callisto. American Astronomical Society, DPS

meeting #42, #54.05; *Bulletin of the American Astronomical Society*, Vol. 42, p.1075.

Zhang, R.H., Li, Z.L., Tang, X.Z., Sun, X.M., Su, H.B., Zhu, C., Zhu, Z.L., (2004). Study of emissivity scaling and relativity of homogeneity of surface temperature. *International Journal of Remote Sensing*. 25, 245–259.

Zhang, L., Zhang, N., Zhao, F., & Chen, Y. (2004). A genetic-algorithm-based experimental technique for determining heat transfer coefficient of exterior wall surface. *Applied Thermal Engineering* 24, 339–349.

VITA

Iryna Danilina was born in Kharkiv, Ukraine on August 3rd, 1981. She graduated from National Technical University "Kharkiv Polytechnic Institute" with the equivalent of a U.S. degree of Master in Applied Mathematics in February of 2004. She started her graduate study at University of Washington, Seattle in 2005.